
1 • Introduction

The first application of nuclear magnetic resonance spectroscopy (NMR, sometimes referred to as n.m.r. in old-fashioned texts) to a biological sample was reported¹ in 1954 by Jacobson, Anderson, and Arnold on the effect of hydration of deoxyribonucleic acid, one year after Watson and Crick's historic discovery. Three years later, Saunders, Wishnia, and Kirkwood obtained the first ¹H NMR spectrum of a protein, ribonuclease.² This spectrum, obtained at 40 MHz, is shown in Fig. 1.1.

In contrast, the 750 MHz ¹H NMR spectrum of the enzyme lysozyme is shown in Fig. 1.2. In the intervening 38 years, the field of NMR spectroscopy has undergone a revolution, culminating in the award of the 1991 Nobel Prize for Chemistry to Richard Ernst, one of the key figures in the development of NMR. However, the recognition given to this field is only just beginning, and the area where the method is likely to have the greatest impact is at the interface between biology, chemistry, and physics. Although there are a number of excellent texts on NMR spectroscopy, they are primarily for chemists, and tend to focus either on the theory of NMR⁵⁻⁶ or on applications to organic chemistry. Those books on biological NMR, while still very useful, tend to be somewhat outdated⁹⁻¹² or directed solely towards structure.¹³ This book seeks to provide a general outline of basic NMR theory and examine selected examples of applications to

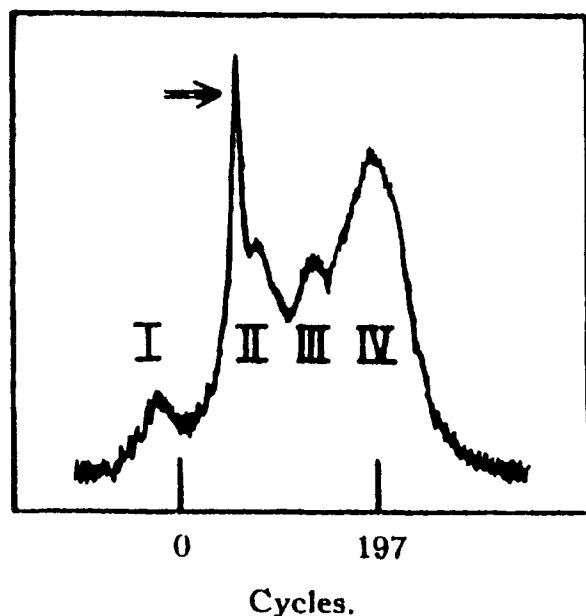


Fig. 1.1 The first ¹H NMR spectrum of an enzyme, ribonuclease, at 40 MHz, obtained in 1957. (Reprinted from Ref. 2 with permission.)

dimensional structures of individual components in the cell, such as proteins, enzymes, DNA, RNA, and membranes. Therefore, a technique which can obtain an image of a human head on the one hand, and the structure of DNA on the other, must be worth learning about.

The following sections will attempt to provide sufficient basic NMR theory for use in solving biological problems. Throughout this book the emphasis will be on molecular details rather than macroscopic details such as the images obtained with MRI. There are a number of excellent texts on the MRI technique, and the reader is referred to those for more information.¹⁴⁻¹⁵

1.1 BASIC THEORY OF NMR

This chapter attempts to provide a brief summary of the salient features of basic NMR theory. It does not presume to be exhaustive, and the reader should refer to one or more of the increasing number of texts in this area for more detailed information (*vide supra*). In our treatment of NMR theory we have chosen to introduce both classical vector formalism and also quantum mechanical Cartesian product operator formalism. In our experience vector formalism, while being extremely useful for simple experiments, is not very helpful in understanding multidimensional NMR experiments. Rather than introduce the far more complicated density operator formalism, we make no apology for adopting the product operator formalism where appropriate. The mathematics follows simple rules, and, while sometimes generating lengthy expressions, algorithms are even available^{16,17} for computer programs such as Mathematica. The product operator formalism is relatively straightforward and very powerful, and is now the method of choice for evaluating new pulse sequences. It is important for researchers using NMR to be familiar with it.

1.1.1 The NMR phenomenon

The magnetic resonance phenomenon occurs as a result of the quantum mechanical property of spin. This is a source of angular momentum intrinsic to a number of different nuclei. The spin angular momentum confers a magnetic moment on a nucleus and therefore a given energy in a magnetic field. The nuclear spin (I) can have the values $I=0$, $\frac{1}{2}$, 1 , $1\frac{1}{2}$, . . . , etc. (see Table 1.1).

Note that common biological nuclei such as ^{12}C or ^{16}O have $I=0$ and therefore do not give NMR spectra. The nuclear magnetic moment (μ) is given by:

$$\mu = \gamma I \hbar \quad (1.1)$$

The gyromagnetic ratio (also known as the magnetogyric ratio) γ is the proportionality constant which determines the resonant frequency of the nucleus for a given external field. Typical nuclei of interest in biological NMR are given in Table 1.2. In a magnetic field, a nucleus of spin I has $2I + 1$ possible orientations, given by the value of the magnetic quantum number m_I , which has values of $-I, -I+1, \dots, I-1$ (e.g. for a nucleus of spin $\frac{3}{2}$, $m_I = -\frac{3}{2}, -\frac{1}{2}, \frac{1}{2}, \frac{3}{2}$). We can regard a spin- $\frac{1}{2}$ nucleus as a small bar magnet, which when placed in a static field has an energy which varies with orientation to the field. The possible energies are quantized, with the two possible values of $m_I(\pm\frac{1}{2})$ corresponding to parallel and antiparallel orientations of this small magnet and the external field. As we shall see

Table 1.1

Mass no.	Atomic no.	I
Odd	Even or odd	$\frac{1}{2}, \frac{3}{2}, \frac{5}{2} \dots$
Even	Even	0
Even	Odd	1, 2, 3 ...

shortly, the NMR absorption is a consequence of transitions between the energy levels stimulated by applied radiofrequency (RF) radiation.

Although we should bear in mind the quantized nature of nuclear spin, we can describe the motion of a nucleus in a magnetic field in terms of classical mechanics. In the presence of an applied magnetic field \mathbf{B}_0 , the magnetic moment experiences a torque which is the vector product of the nuclear angular momentum \mathbf{J} and the magnetic moment μ (see Fig. 1.3). Note, however, that the physical picture presented here does not represent reality. The findings of the famous Stern–Gerlach experiment clearly suggest that spin angular momentum is quantized, and therefore classical mechanics is not applicable. Furthermore, the nucleus is not necessarily spinning about its axis—indeed were it to be spinning the radial velocity would exceed the speed of light. Thus although we speak of ‘spin’ as if the nucleus were actually rotating about its axis, this is an unfortunate choice of words since the source of the magnetic moment is a purely quantum mechanical property which could just as easily be called ‘sweetness’, ‘bitterness’, or whatever.

According to Newtonian mechanics, this torque equals the rate of change of angular momentum:

$$\frac{d\mathbf{J}}{dt} = \boldsymbol{\mu} \times \mathbf{B}_0 \quad (1.2)$$

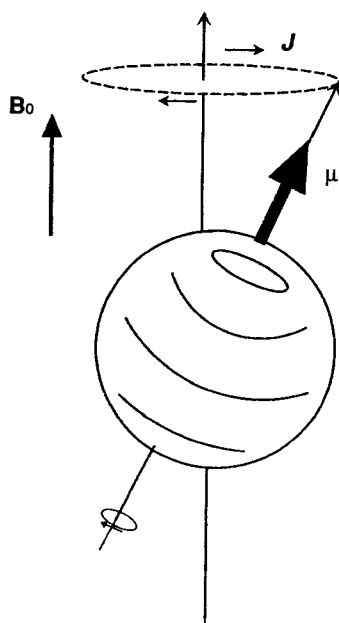


Fig. 1.3 Schematic representation of the motion of a nucleus in a magnetic field.

Table 1.2 Magnetic properties of some biologically useful nuclei

Isotope	Spin	Natural abundance (%)	Quadrupole moment Q (10^{-28} m ²)	Gyromagnetic ratio γ (10^7 rad s ⁻¹ T ⁻¹)	Sensitivity rel. ^a	abs. ^b	NMR-frequency (MHz) at a field (T) of 2.3488
¹ H	1/2	99.98	—	26.7522	1.00	1.00	100.000
² H	1	1.5×10^{-2}	2.87×10^{-3}	4.1066	9.65×10^{-3}	1.45×10^{-6}	15.351
³ H	1/2	0	—	28.5350	1.21	0	106.663
⁷ Li	3/2	92.58	-3.7×10^{-2}	10.3976	0.29	0.27	38.863
¹¹ B	3/2	80.42	4.1×10^{-2}	8.5847	0.17	0.13	32.084
¹³ C	1/2	1.108	—	6.7283	1.59×10^{-2}	1.76×10^{-4}	25.144
¹⁴ N	1	99.63	1.67×10^{-2}	1.9338	1.01×10^{-3}	1.01×10^{-3}	7.224
¹⁵ N	1/2	0.37	—	-2.7126	1.04×10^{-3}	3.85×10^{-6}	10.133
¹⁷ O	5/2	3.7×10^{-2}	-2.6×10^{-2}	-3.6280	2.91×10^{-2}	1.08×10^{-5}	13.557
¹⁹ F	1/2	100	—	25.1815	0.83	0.83	94.077
²³ Na	3/2	100	0.10	7.0704	9.25×10^{-2}	9.25×10^{-2}	26.451
²⁵ Mg	5/2	10.13	0.22	-1.6389	2.67×10^{-3}	2.71×10^{-4}	6.1195
³¹ P	1/2	100	—	10.8394	6.63×10^{-2}	6.62×10^{-2}	40.481
³⁵ Cl	3/2	75.53	-8.2×10^{-2}	2.6242	4.70×10^{-3}	3.55×10^{-3}	9.798
³⁹ K	3/2	93.1	5.5×10^{-2}	1.2499	5.08×10^{-4}	4.73×10^{-4}	4.667
⁴³ Ca	7/2	0.145	-5×10^{-2}	-1.8028	6.40×10^{-3}	9.28×10^{-6}	6.728
⁵¹ V	7/2	99.76	2.17×10^3	-5.2×10^{-2}	0.38	0.38	26.289
⁵⁷ Fe	1/2	2.19	—	0.8687	3.37×10^{-5}	7.38×10^{-7}	3.231
⁷⁵ As	3/2	100	0.29 ^v	4.5961	2.51×10^{-2}	2.51×10^{-2}	17.126
⁷⁷ Se	1/2	7.58	—	5.1214	6.93×10^{-3}	5.25×10^{-4}	19.067
¹¹³ Cd	1/2	12.26	—	-5.9609	1.09×10^{-3}	1.33×10^{-3}	22.182

^aAt constant field for equal number of nuclei.^bProduct of relative sensitivity and natural abundance.

$$\mathbf{J} = I\hbar \quad (1.3)$$

$$\therefore \frac{d\boldsymbol{\mu}}{dt} = \boldsymbol{\gamma}\boldsymbol{\mu} \times \mathbf{B}_0 \quad \text{using} \quad \boldsymbol{\mu} = \boldsymbol{\gamma}I\hbar = \boldsymbol{\gamma}\mathbf{J} \quad (1.4)$$

This equation is analogous to the equation of motion for a body with angular momentum \mathbf{L} in a gravitational field \mathbf{g} with mass m at a distance \mathbf{r} from the fixed point of rotation, if we equate \mathbf{J} to \mathbf{L} and \mathbf{B}_0 to \mathbf{g} , and regard $\mathbf{r} \times m$ as an intrinsic property of the body analogous to $\boldsymbol{\gamma}\boldsymbol{\mu}$:

$$\frac{d\mathbf{L}}{dt} = \mathbf{r} \times m\mathbf{g} \quad (1.5)$$

Thus this is just like the motion of a gyroscope which in a gravitational field precesses, i.e. its axis of rotation itself rotates about the field direction. In the classical analogy, the same motion occurs for nuclear spins in a magnetic field.

The energy of the interaction is proportional to $\boldsymbol{\mu}$ and \mathbf{B}_0 (see Fig. 1.4), so

$$E = -\boldsymbol{\gamma}\hbar m_l \mathbf{B}_0 \quad (1.6)$$

and since $\Delta m_l = 1$,

$$\Delta E = \boldsymbol{\gamma}\hbar \mathbf{B}_0 \quad (1.7)$$

and from Planck's law,

$$\Delta E = h\nu \quad (1.8)$$

then

$$\nu = \frac{\boldsymbol{\gamma}\mathbf{B}_0}{2\pi} \quad (\text{in Hz}) \quad (1.9)$$

or

$$\omega = \boldsymbol{\gamma}\mathbf{B}_0 \quad (\text{in rad s}^{-1}) \quad (1.10)$$

Note that we have dropped the minus sign between Equations (1.6) and (1.7). This is a convention that has been widely adopted for convenience in the NMR literature, although, as pointed out by Ernst and co-workers,⁴ strictly speaking, $\omega = -\boldsymbol{\gamma}\mathbf{B}_0$, which

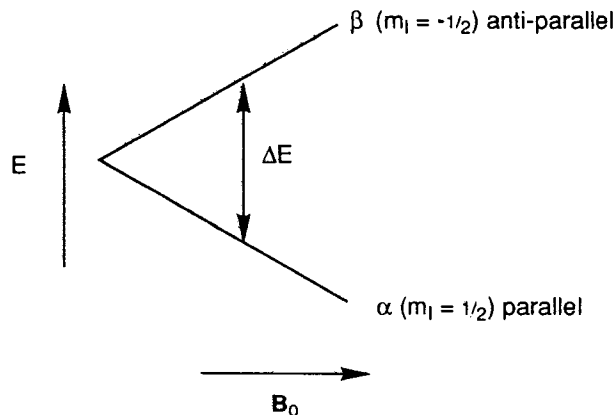


Fig. 1.4 Energy level diagram.

has consequences for the Cartesian representation of vectors and product operators considered in Sections 1.1.2 and 1.1.3. Thus nuclei precess around the \mathbf{B}_0 axis at a speed which is called the Larmor frequency (which is its NMR absorption frequency, ω). The rotation may be clockwise or anticlockwise depending on the sign of γ , but is always the same for any particular nucleus.

The two energy states α and β will be unequally populated, the ratio being given by the Boltzmann equation:

$$\frac{N_\beta}{N_\alpha} = e^{-\Delta E/k_B T} \quad (1.11)$$

Another way to look at this is that in a sample containing a large number of spins, all possessing the same Larmor frequency, the parallel orientation of the z component of each spin along the \mathbf{B}_0 direction is of lower energy than the antiparallel one. So at thermal equilibrium, we expect the Boltzmann surplus as shown in Fig. 1.5. Thus along the z axis there is a net magnetization of the sample parallel to the field. All the contributing spins have components precessing in the xy plane, but because all have equal energy, the phase of the precession is random. Thus for an ensemble of spins, there is no net magnetization in the xy plane and total magnetization of the sample is stationary and aligned with the z axis (called \mathbf{M}_0).

1.1.2 The vector model

Radio frequency (RF) radiation is electromagnetic (see Fig. 1.6) and can be represented as an oscillating magnetic field, which in turn can be represented by magnetization vectors (see Fig. 1.7). This represents the half cycle of the oscillation of the magnetization due to the presence of the RF (also known as the \mathbf{B}_1) field. Alternatively, we can represent it as two magnetization vectors of constant amplitude rotating about an axis (x) in opposite directions, with angular frequency = RF. Thus this pair of counter-rotating vectors is a valid way of representing the RF (see Fig. 1.8).

So when the sample and the RF field interact, we have a moving field interacting with a static one (although this, too, causes precessional motion in the sample). Conceptually, the way this rather complex picture is simplified is by rotating the coordinate axes at the same rate as the nuclear precession. Now since there is no precession, it looks as though the applied field (which caused the precession) has disappeared. However, the net magnetization remains along the z axis. Furthermore, the RF can be decomposed into two

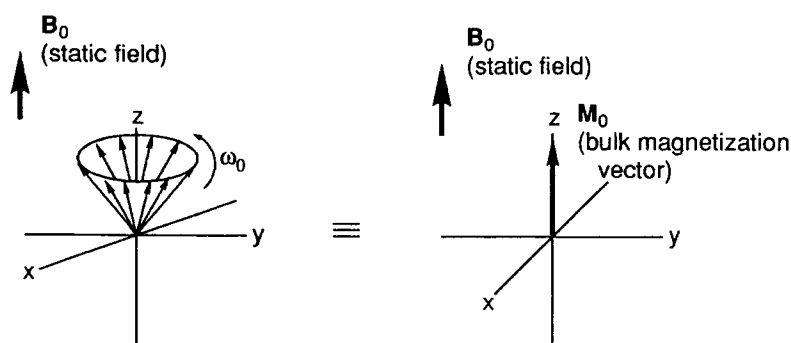


Fig. 1.5 The bulk magnetization vector.

components, one in the xy plane. The other, which was originally moving at an equal speed in the opposite direction, is rotating in the new frame at twice the Larmor frequency. This can now be neglected, and has no effect on the NMR experiment (see Fig. 1.9). When a pulse of RF is applied to the sample, i.e. the \mathbf{B}_1 field is switched on and then switched off, in the rotating frame the \mathbf{M}_0 and \mathbf{B}_1 vectors are static and orthogonal. This generates a torque and the sample magnetization is driven around by the \mathbf{B}_1 vector, at a speed dependent on the field strength. Thus we could move it through 90° , as shown in Fig. 1.10. Note that the direction of motion (in this case clockwise relative to the \mathbf{B}_1 direction) is to some extent arbitrary, and in general the NMR literature using classical vector formalism adopts the convention used here (although the opposite convention has

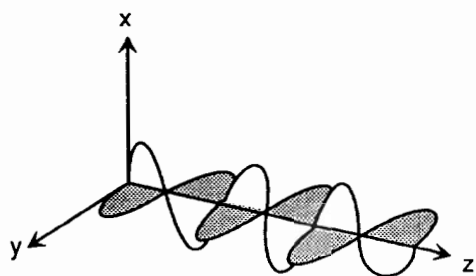


Fig. 1.6 Electromagnetic nature of RF radiation with oscillating magnetic and electric fields.

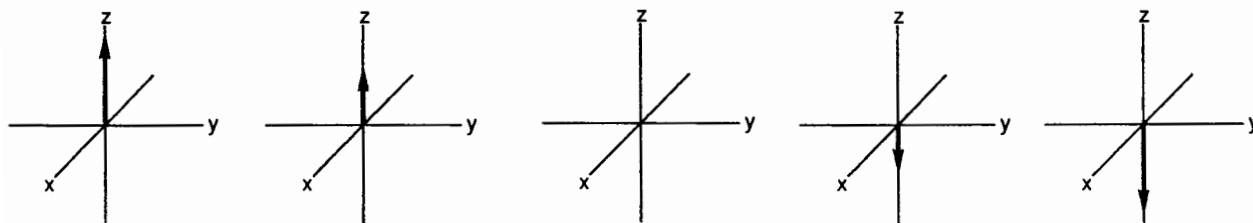


Fig. 1.7 RF radiation represented by magnetization vectors.

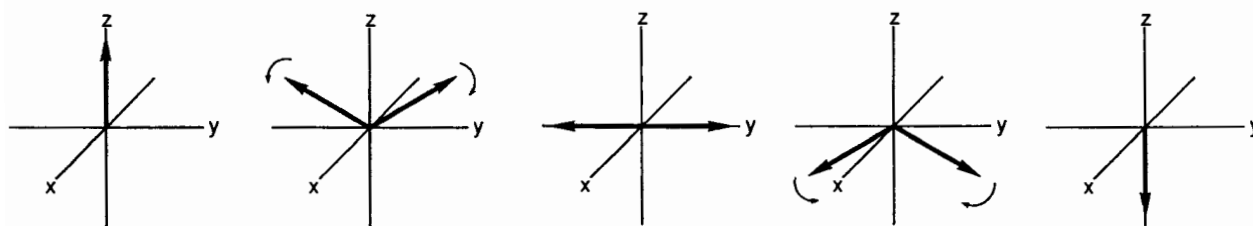


Fig. 1.8 RF radiation represented by two counter rotating vectors.

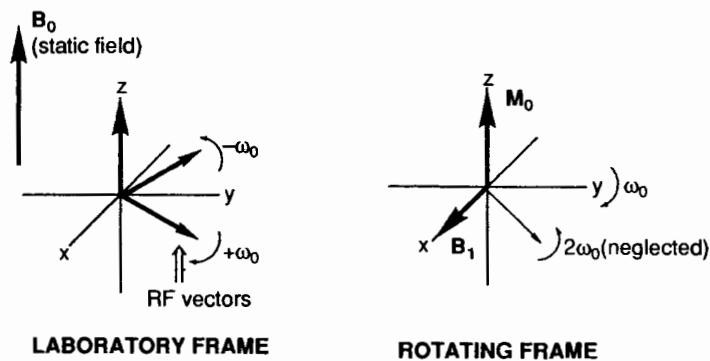


Fig. 1.9 Magnetization vectors shown in the laboratory and rotating frames.

been adopted when using the Cartesian representation of product operators—see Section 1.1.3). Note, however, that the direction is governed by the sign of the gyromagnetic ratio. After the pulse has finished, the sample magnetization remains in the xy plane. In the laboratory frame it precesses about the static field, generating radio signals (see Fig. 1.11). These radio signals generate what is called the *free induction decay* (FID), which is a function that decays exponentially with time (see Fig. 1.12). The FID is related to the frequency domain spectrum through *Fourier transformation*. This is as follows:

$$f(\omega) = \int_{-\infty}^{\infty} f(t)e^{i\omega t} dt \tag{1.12}$$

$$\text{Re}(f(\omega)) = \int_{-\infty}^{\infty} f(t)\cos \omega t dt$$

$$\text{Im}(f(\omega)) = \int_{-\infty}^{\infty} f(t)\sin \omega t dt \tag{1.13}$$

since $e^{i\omega t} = \cos \omega t + i \sin \omega t$ (see Fig. 1.13). This is a consequence of the fact that every NMR signal has amplitude, frequency, *and* phase. The NMR signal is detected using a

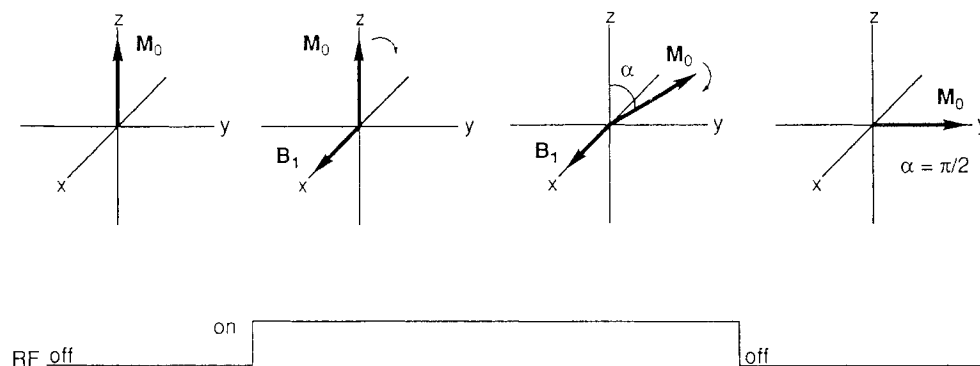


Fig. 1.10 The sample magnetization driven to the y axis after a 90° pulse.

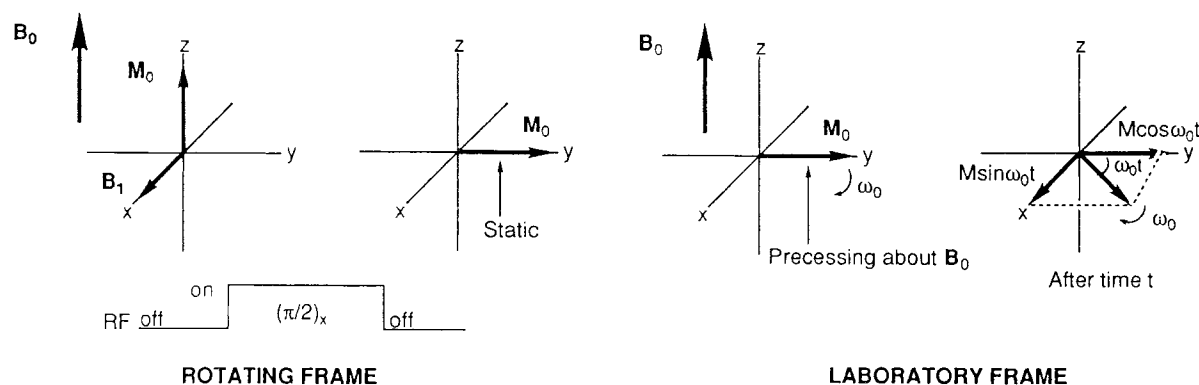


Fig. 1.11 Precession of the sample magnetization about the static field.

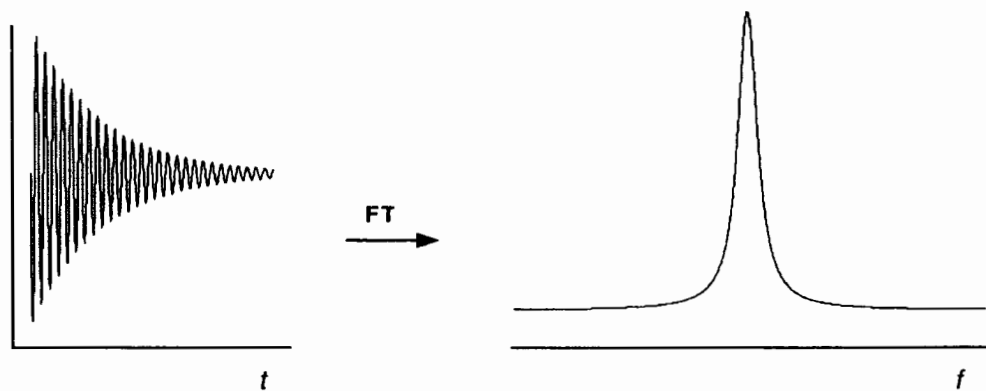


Fig. 1.12 The free induction decay.

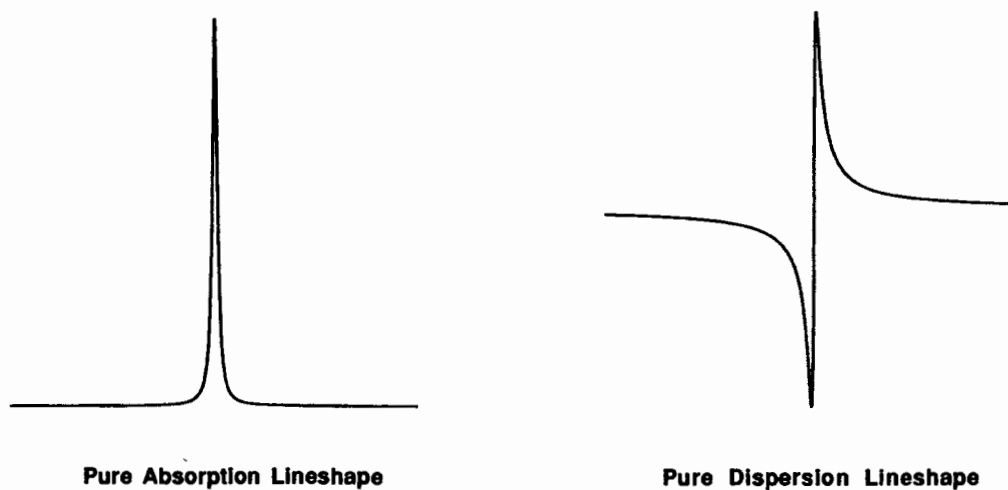


Fig. 1.13 Pure absorption lineshape versus pure dispersion lineshape.

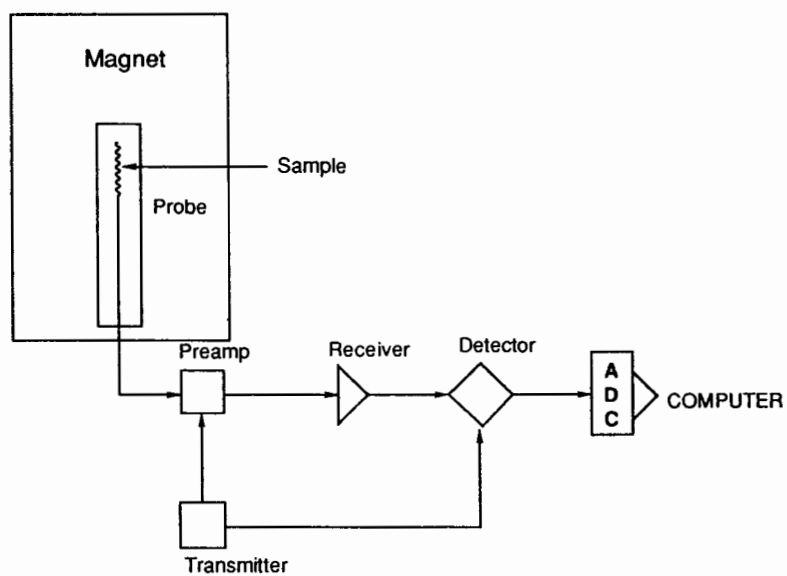


Fig. 1.14 Outline of a NMR spectrometer.

detector, and the basic outline of an NMR spectrometer is given in Fig. 1.14. This represents a greatly simplified picture of a modern NMR spectrometer, which nowadays is commonly equipped with three RF channels and an array of sophisticated equipment, a discussion of which is outside the scope of this book. However, one feature which is particularly important is the way in which the signal is detected. Here a technique known as *quadrature detection* is used. The detectable magnetization can be represented as a vector precessing in the xy plane, as we saw in Fig. 1.9, so that a detector aligned along the x axis would be insensitive to the direction of rotation of the vector. In other words, the detector cannot distinguish whether the signal frequency is greater or less than the reference frequency in the case where two signals are on opposite sides of the reference by the same frequency difference. The two vectors would be rotating at the same frequency but in opposite directions. In order to distinguish between these we use a detector that can detect the signals along both the y and x axes simultaneously. Instead of having two coils, however, the signal is manipulated electronically, by having two detectors in which one has had the phase of the reference frequency shifted by 90° and the FIDs stored in separate memory locations in the computer. Since the phase of one of these FIDs is affected by the sign of the frequency, these two FIDs correspond to the real and imaginary components of the signal, and are treated as such in the Fourier transformation.

The question of *phase* both in terms of the transmitter pulses and in terms of the receiver is important. In many pulse sequences, as we shall see later in this chapter and in Chapter 2, elaborate phase cycling of pulses and the receiver are required in order to achieve the particular result desired. This is the means by which desired and undesired signals are separated. The same result can also be achieved using what are called *pulsed field gradients*, which are emerging as an important and fast alternative to lengthy phase cycles.¹⁸ An example of the consequence of changing the phase of the transmitter pulses is summarized in Fig. 1.15, which uses the vector model to represent the four possible phases (x , y , $-x$, and $-y$).

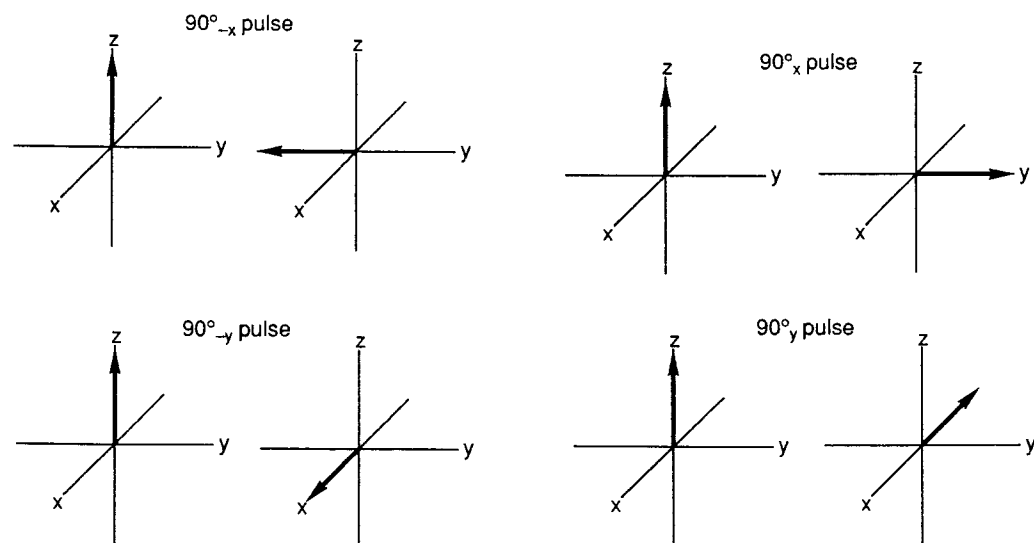


Fig. 1.15 The vector representation of RF pulses of differing phase.

1.1.3 The product operator

There are intrinsic limitations in representing the effects of RF pulses in NMR using vectors, and we need to consider alternative ways of looking at this. In contrast to the vector formalism, in which the macroscopic magnetization rotates under the influences of pulses, and/or precesses under the influence of chemical shift, the entire state of the spins or spin system can be described by the wave function, $\Psi(t)$, or the density operator $\sigma(t)$. Disregarding relaxation, the time evolution of the density operator is described by the Liouville–von Neumann equation:

$$\frac{d\sigma(t)}{dt} = -i[\mathcal{H}(t), \sigma(t)] \quad (1.14)$$

$\mathcal{H}(t)$ is the famous Hamiltonian operator, which includes chemical shift terms, coupling terms, and so on. Instead of getting into the rather complex area of density matrices, we can describe the density operator in terms of Cartesian *product operators*.¹⁹ Thus the ground state of a system at thermal equilibrium is described by a *polarization* (or population—see Section 1.1.7) along the z axis, I_z . After a pulse in the y direction:

$$I_x \xrightarrow{\alpha I_y} I_x \cos \alpha - I_z \sin \alpha \quad (1.15)$$

$$I_y \xrightarrow{\alpha I_y} I_y \quad (1.16)$$

$$I_z \xrightarrow{\alpha I_y} I_z \cos \alpha + I_x \sin \alpha \quad (1.17)$$

These Cartesian operators, I_x , I_y , and I_z transform like magnetizations when a rotation is performed. The properties of a state I_x , I_y , and I_z can be read off directly with such simple operators, since they each consist of only one operator. I_x is associated with an x magnetization, and I_y and I_z accordingly.

We will adopt the following convention:

$\alpha I_{x,y}$ or αI_ϕ = flip angle α about an axis in the xy plane (forming an angle ϕ with the x axis)

$\Omega I_z t$ = evolution of chemical shift Ω of nucleus I during time t

$2\pi \mathcal{J} I_{1z} I_{2z} t$ = evolution of coupling \mathcal{J} between nuclei I_1 (or I) and I_2 (or S) during time t

So for chemical shifts:

$$I_x \xrightarrow{\Omega t I_z} I_x \cos \Omega t + I_y \sin \Omega t \quad (1.18)$$

$$I_y \xrightarrow{\Omega t I_z} I_y \cos \Omega t - I_x \sin \Omega t \quad (1.19)$$

$$I_z \xrightarrow{\Omega t I_z} I_z \quad (1.20)$$

Detection of x magnetization leads to build-up of the signal according to the coefficient $-\sin \Omega t$ of I_x . Fourier transformation leads to a line at $\pm \Omega$. Quadrature detection allows selection at either $+\Omega$ or $-\Omega$. Thus we can summarize the *vector model* and the *product operator model* as in Fig. 1.16 for a simple 90° pulse. The effects of chemical shifts, pulses, and positive scalar couplings on product operators are summarized pictorially in Fig. 1.17, and summarized mathematically in Appendix 1. Note that the sense of rotation for product operators is opposite to the classical description presented in Section 1.1.2. As

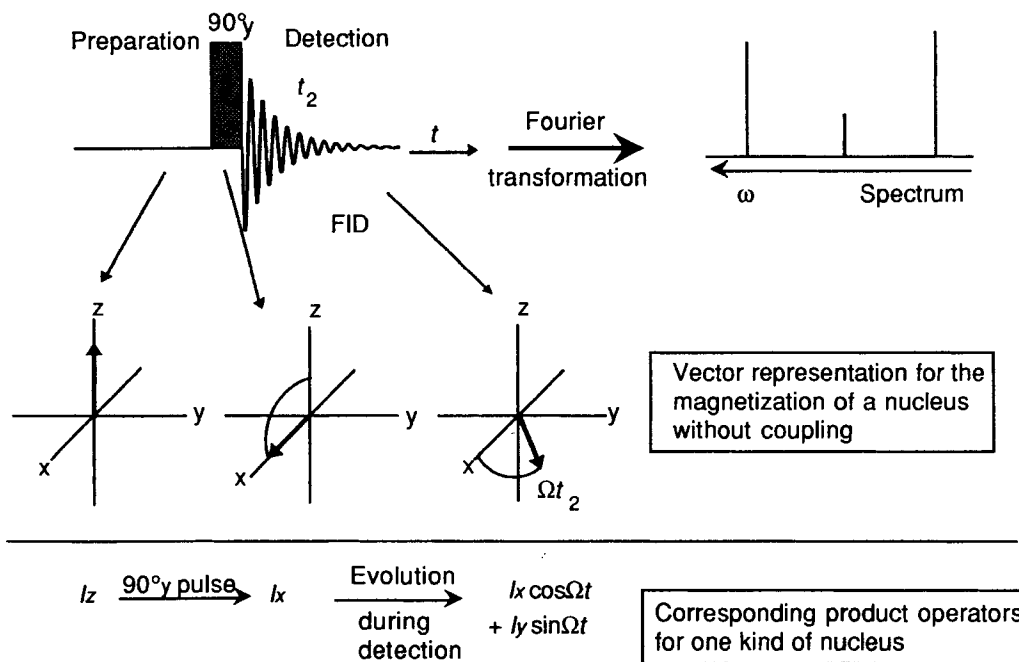


Fig. 1.16 The vector model and the product operator model for a 90° pulse.

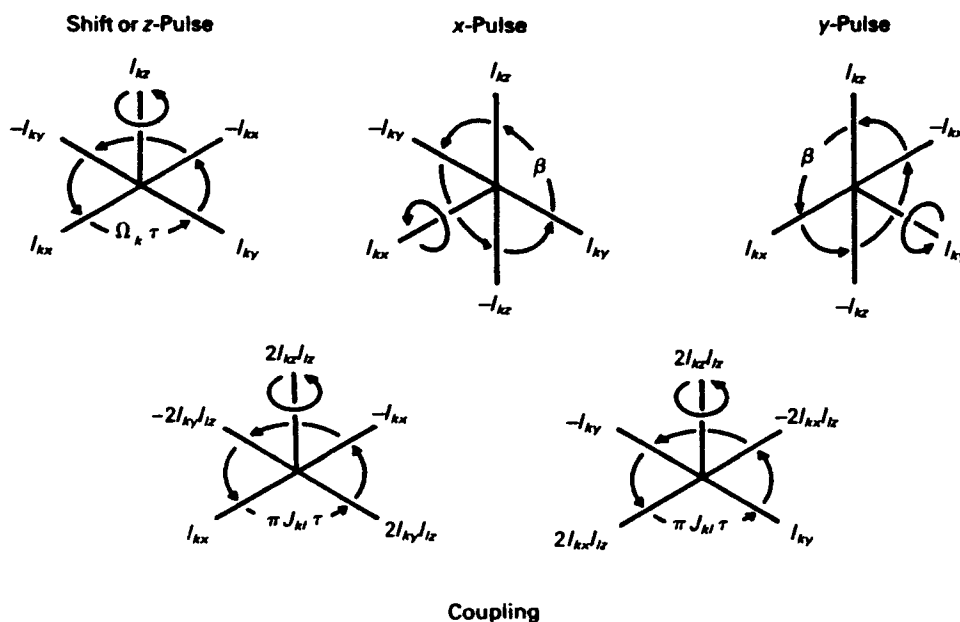


Fig. 1.17 Graphic representation of the effect of chemical shifts, pulses, and positive scalar couplings on product operators. (Reprinted from Ref. 4 with permission.)

mentioned in Section 1.1.1, this results from the fact that, strictly speaking, $\omega = -\gamma\mathbf{B}_0$, and when product operator formalism was introduced, the minus sign was retained, thereby changing the sense of the rotation relative to classical formalism. Of course this has nothing to do with the physics, and is simply a consequence of how the equations are written.

1.1.4 Relaxation

Having considered how we obtain xy magnetization, let us turn to what happens to it after the RF pulse is switched off. Naturally, it might be expected to return eventually to thermal equilibrium along the z axis. The time it takes to do this is relatively long compared to other spectroscopic techniques, and constitutes an important aspect of the experiment.

In the Bloch theory of relaxation, the assumption is made that equilibrium will be approached exponentially. Thus magnetization will build up (or decay) according to:

$$\frac{dM_z}{dt} = \frac{M_0 - M_z}{T_1} \quad (1.21)$$

$$\frac{dM_x}{dt} = -\frac{M_x}{T_2} \quad (1.22)$$

$$\frac{dM_y}{dt} = -\frac{M_y}{T_2} \quad (1.23)$$

Longitudinal relaxation (T_1)

The build-up of M_0 can be represented as shown in Fig. 1.18. Thus if M_0 is the magnetization at thermal equilibrium, then

$$M_z = M_0(1 - e^{-t/T_1}) \quad (1.24)$$

T_1 is called the longitudinal (or spin-lattice) relaxation. After a $\pi/2$ pulse, the magnetization precesses about the z axis in the xy plane. With longitudinal relaxation, the

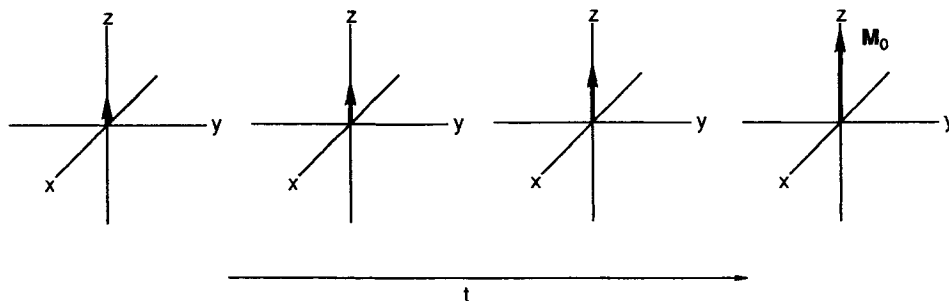


Fig. 1.18 Build-up of magnetization (M_0).

z magnetization reappears (see Fig. 1.19) with the time constant T_1 . One common method for the measurement of T_1 s is the *inversion-recovery* method, which is shown in Fig. 1.20.

Transverse relaxation (T_2)

The transverse relaxation, or T_2 , is not intuitively obvious, and is harder to understand in simple physical terms. When the magnetization is in the xy plane, there is *phase coherence* between the spins in the transverse plane, and loss of this phase coherence due to mutual exchange of spin energies is what gives rise to T_2 relaxation. However, in general, T_2 is always greater than T_1 , and this is because there are additional causes of loss of transverse magnetization. Disregarding longitudinal relaxation (T_1) for a moment, the static magnetization in the xy -plane would not remain there because of another simple fact: the static field is not uniform throughout the sample. Thus, if we divide up the sample into small regions such that the field is uniform (regions known as *isochromats*), then the total magnetization is the sum of all these regions, each of which contributes a precessing vector which differs slightly in frequency. This blurs the bulk magnetization vector, and this is due to inhomogeneous broadening, which often dominates the transverse (or spin-spin) relaxation, T_2 . Note that the magnetic field inhomogeneity is really an experimental artefact, and when it dominates T_2 the directly observed decay is usually defined as T_2^* whereas T_2 is usually reserved for other causes of loss of order (see Fig. 1.21).

Spin echoes

One of the fascinating things that happens if we apply two RF pulses in quick succession relative to T_1 is the production of a spin echo. Consider the pulse sequence $(\pi/2) - \tau - \pi$ shown in Fig. 1.22. After the $\pi/2$ pulse, the inhomogeneity causes the isochromats to fan

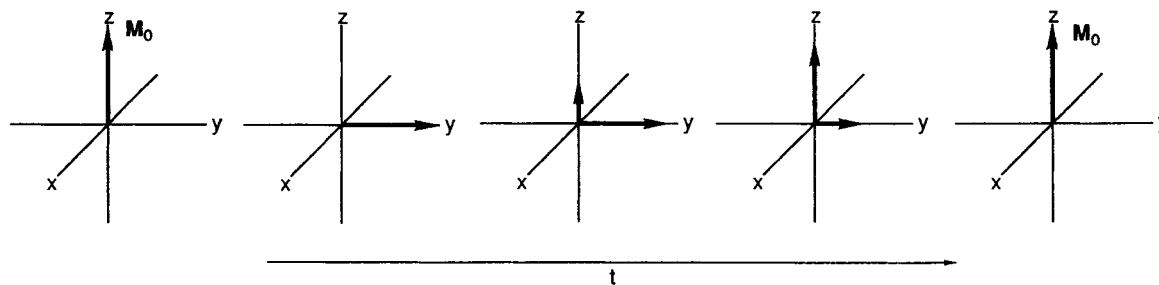


Fig. 1.19 Reappearance of the z -magnetization.

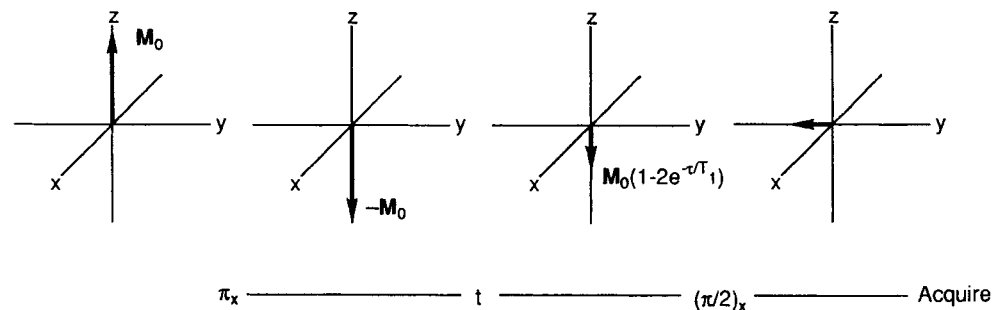


Fig. 1.20 The inversion recovery method.

out. The front edge is labelled ‘+’ for the vectors precessing faster than ω_0 , and the back edge is labelled ‘-’ for the slower vectors. The π_x pulse rotates all the isochromats together about the x axis, leaving the vectors on the y axis. Now the ‘+’ sign lags behind the average direction of the vectors and the ‘-’ side is ahead. Thus the faster vectors catch up with the average position and the slow ones fall back to it. Thus after an additional time they refocus to give an echo. In fact, in a sense, *time has been reversed*, since the disorder in the system can be reversed.²⁰

Let us also consider the product operator calculation for this pulse sequence:

$$\begin{aligned}
 \sigma_0 &= I_z \\
 &\downarrow 90_x \\
 \sigma_1 &= -I_y \\
 &\downarrow \Omega\tau I_z \\
 \sigma_2 &= -I_y \cos \Omega\tau + I_x \sin \Omega\tau \\
 &\downarrow 180_y \\
 \sigma_3 &= -I_y \cos \Omega\tau - I_x \sin \Omega\tau \\
 &\downarrow \Omega\tau I_z \\
 \sigma_4 &= -I_y \cos^2 \Omega\tau + I_x \cos \Omega\tau \cdot \sin \Omega\tau - I_x \cos \Omega\tau \cdot \sin \Omega\tau - I_y \sin^2 \Omega\tau \\
 &\downarrow \\
 \sigma_4^{\text{obs}} &= -I_y
 \end{aligned}$$

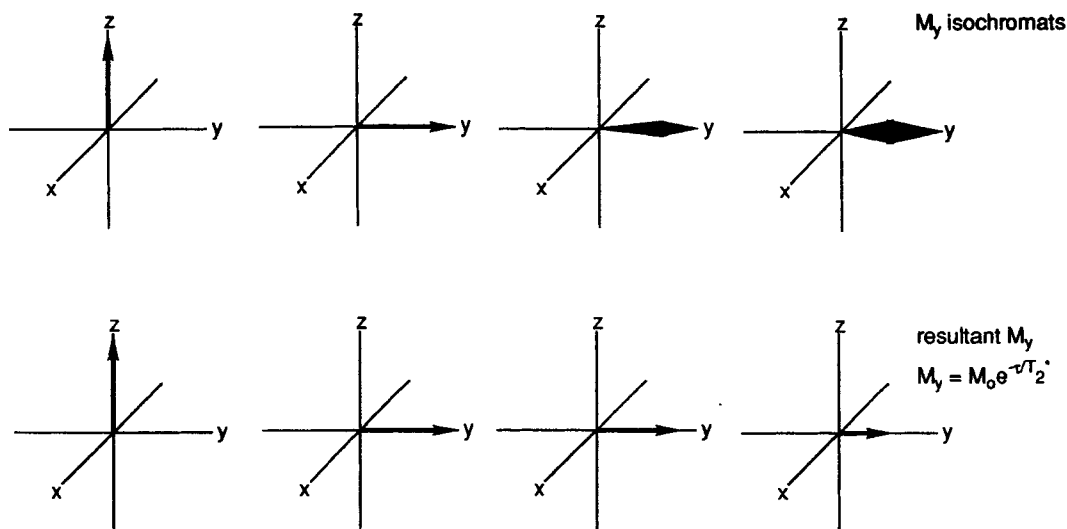


Fig. 1.21 The vector model of transverse relaxation (T_2).

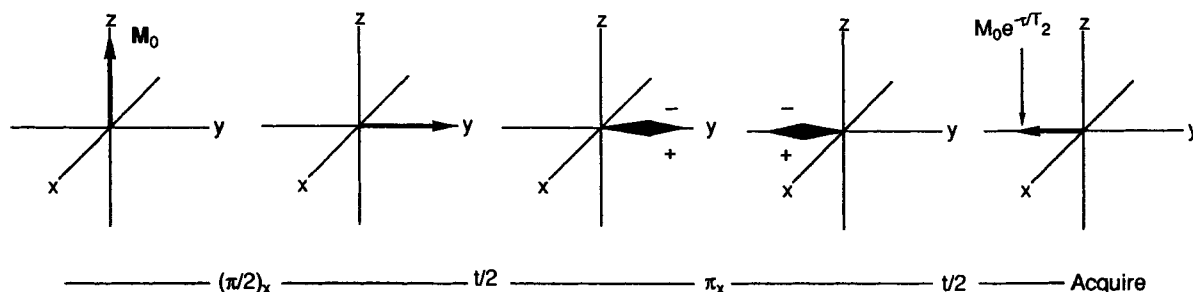


Fig. 1.22 The spin echo method.

So note that we have essentially returned to where we started after the first 90° pulse. Remembering this point greatly simplifies product operator calculations, since many pulse sequences use spin echo sequences to refocus chemical shifts.

Spin echoes play a very important role in modern NMR experiments. For example, two lines of different chemical shifts evolve at different rates in the rotating frame, so if we apply an echo sequence, they diverge before the 180° pulse, but realign after it. Similarly, heteronuclear couplings are refocused by spin echoes, but *not* homonuclear couplings. Spin echoes can be used to measure T_2^* s, although there are inherent difficulties in such measurements. An alternative method is to simply measure the linewidth, since $\nu_{1/2} = 1/\pi T_2^*$, where $\nu_{1/2}$ is the linewidth at half-height.

Another spin echo sequence, and the one usually used in practice, is the Carr–Purcell–Meiboom–Gill spin echo sequence, which is:

$$(\pi/2)_x - \tau - \pi_y - 2\tau - \pi_y - 2\tau - \pi_y - \dots$$

Cumulative errors due to an incorrectly set pulse length do not arise. We can illustrate this if we consider the fate of the fastest moving isochromat only and look at the consequence of the pulse angle being not π but some slightly different value $\pi - \epsilon$, as shown in Fig. 1.23. Consider a pulse $\theta = \pi - \epsilon$, which is slightly shorter than π and directed along the y axis. The pulse interchanges the orders of rotation of the slow and fast magnetization isochromats (Fig. 1.23(c)), and leaves them slightly above the xy plane. Refocusing then occurs normally at time 2τ but takes place above the y axis in the zy plane (Fig. 1.23(d)). After the dephasing period τ (Fig. 1.23(e)) the second $\pi - \epsilon$ pulse rotates the isochromats

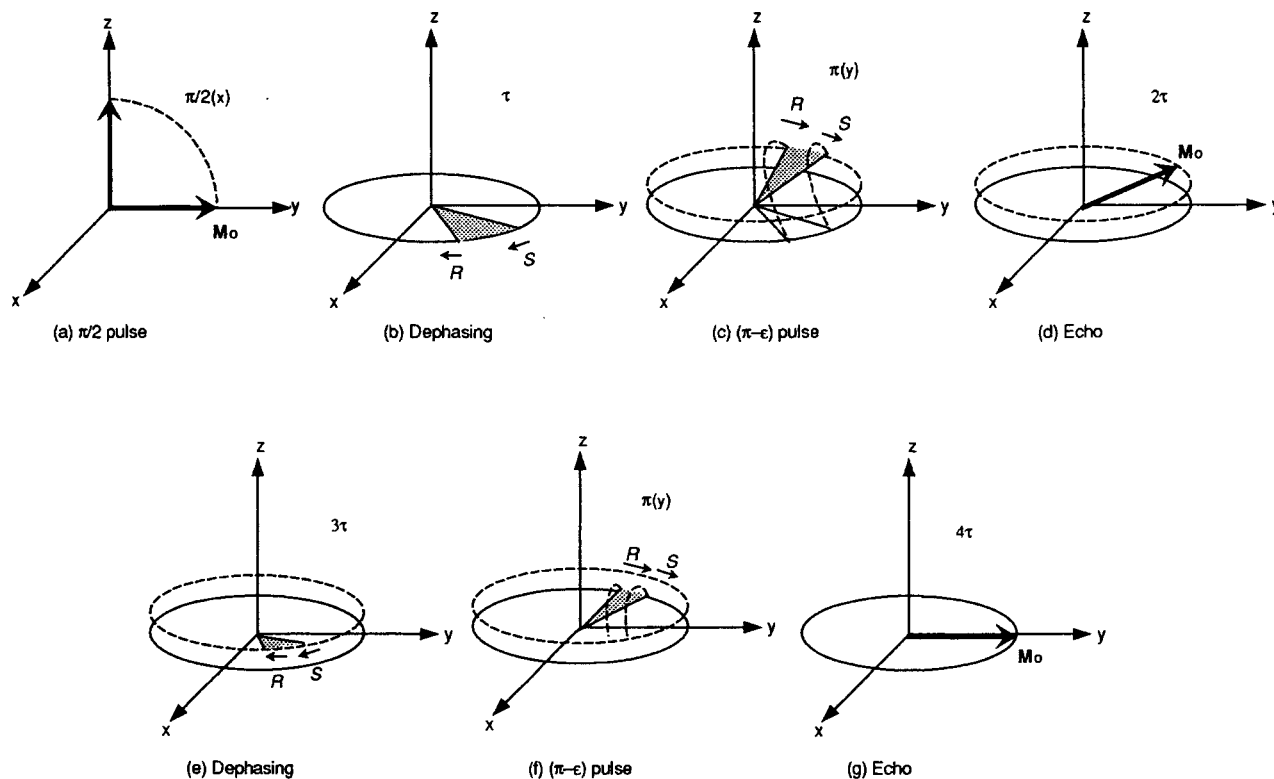


Fig. 1.23 Vectorial representation of the Carr–Purcell–Meiboom–Gill spin echo.

exactly back into the xy plane where they are refocused at time 4τ (Fig. 1.23(g)). Thus all the even-numbered echoes are produced along the right direction, y , whereas all the odd-numbered echoes are only slightly displaced and by a constant angle.

1.1.5 The nuclear Overhauser effect

The Nuclear Overhauser Effect (NOE, η) is the change in the intensity of an NMR resonance when the transitions of another are perturbed. Generally, this means saturation, which is the elimination of a population difference across some transitions (by irradiating one with a weak RF field) while observing the signals from others:

$$\eta_i = (I - I_0)/I_0 \quad (1.25)$$

where I_0 is the thermal equilibrium intensity.

Consider two spin- $\frac{1}{2}$ nuclei I and S , with the same γ but different chemical shifts and not \mathcal{J} coupled where the energy levels are represented as combinations of α and β , and the populations indicated with multiples of N . The system is shown in Fig. 1.24. Chemical shifts are very small compared with the Larmor frequency (i.e. of the order of ppm), so the transitions have nearly equal energy. Assuming we have $4N$ nuclei, then each energy level would have N nuclei of almost equal energy. The population differences are given in Table 1.3.

The first four differences in Table 1.3 are across the normal transitions which give rise to the NMR lines, while the other two involve changes in the quantum number M (which is the total of the individual quantum numbers m for the two nuclei). Although these latter two are not observable, they may contribute to the relaxation pathways. Another way of looking at this is to consider how the system restores itself. The relaxation can take place in several ways and we can assume that relaxation across a single transition is first order, and the rate constant is designated W , with the subscript distinguishing the change in M involved (see Fig. 1.25). T_1 is therefore related to some combination of W_1^I , W_2 , and W_0 . If W_2 and $W_0 = 0$, then

$$T_1^I = \frac{1}{2W_1} \quad (1.26)$$

Note that if W_2 and $W_0 \neq 0$ then the total relaxation time for spin I involves transitions of spin S . Thus T_1 measurements on multispin systems are not straightforward.

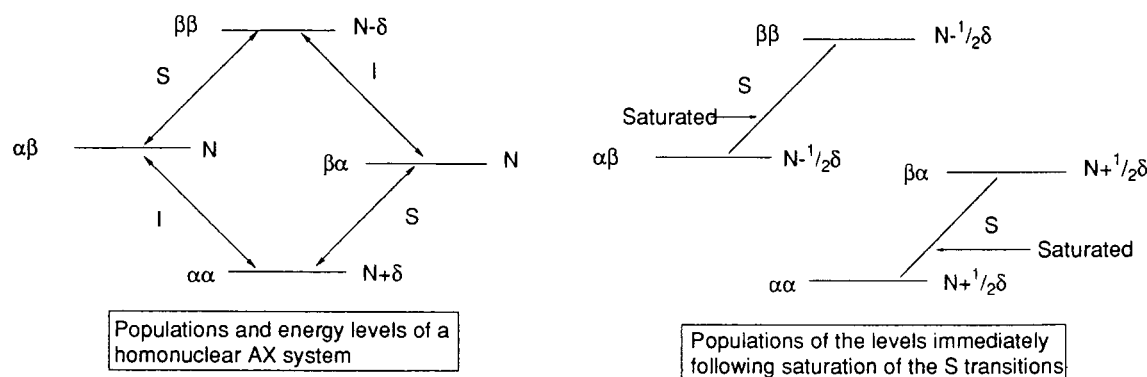


Fig. 1.24 Populations of levels before and after saturation of the S transitions.

Table 1.3 Population differences for transitions between energy levels in one-dimensional NOE experiment

	At thermal equilibrium	After saturation of S
I transitions:	$\left. \begin{array}{l} \alpha\alpha-\alpha\beta \\ \beta\alpha-\beta\beta \end{array} \right\} \delta$	δ
S transitions:	$\left. \begin{array}{l} \alpha\alpha-\beta\alpha \\ \alpha\beta-\beta\beta \end{array} \right\} \delta$	0
$\Delta m=0$ transition:	$\beta\alpha-\alpha\beta$ 0	δ
$\Delta m=2$ transition:	$\alpha\alpha-\beta\beta$ 2δ	δ

If only single-quantum transitions were involved, saturation of spin S would result in no change in intensity for spin I . It is the so-called zero- and double-quantum transitions, W_0 and W_2 that enable us to detect the NOE. If W_0 is the dominant relaxation pathway, saturating S decreases the intensity of the I resonance, and there is a negative NOE at I due to S . Conversely, if W_2 is the dominant relaxation pathway, saturating S increases the intensity of the I resonance, and there is a positive NOE at I due to S .

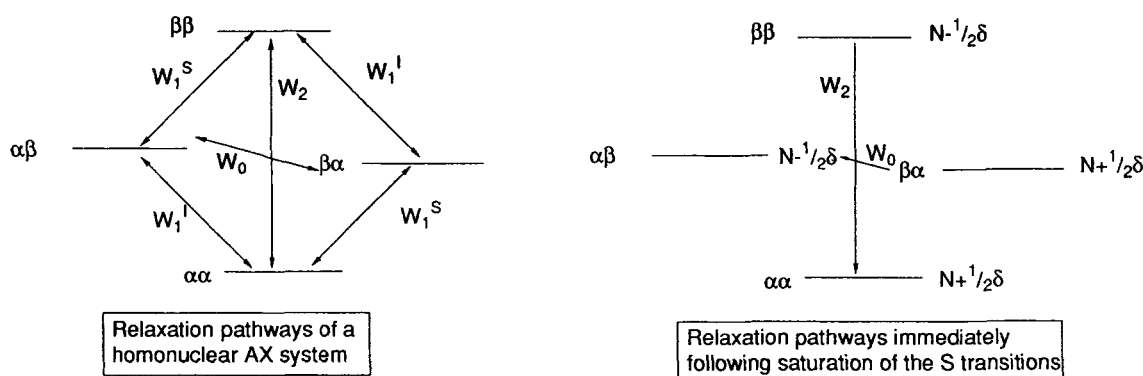
The steady-state NOE enhancement at spin I on saturation of spin S is described by the Solomon equation:²¹

$$\eta_i = \frac{\gamma_S}{\gamma_I} \frac{W_2 - W_0}{2W_1^I + W_2 + W_0} \quad (1.27)$$

Deriving Equation (1.27) is outside the scope of this book, but interested readers should refer to the book by Neuhaus and Williamson.²² Note that for homonuclear NOEs $\gamma_S = \gamma_I$ and typically the maximum enhancement is ≈ 50 per cent whereas for heteronuclear NOEs the enhancement is also multiplied by the ratio of the two γ s.

Mechanisms for relaxation

The interaction which gives rise to the NOE is the dipolar coupling between nuclei. This is the interaction between nuclear magnetic dipoles, in which the local field at one nucleus is due to the presence of the other. Since this local field is dependent upon the orientation of the whole molecule, it may vary from one molecule to the next. In amorphous or

**Fig. 1.25** Relaxation pathways before and after saturation of the S transitions.

polycrystalline solids, where the positions of single molecules are fixed, but vary from one molecule to the next, this leads to a range of resonant frequencies and characteristically broad lineshapes. In single crystals, the lineshape is dependent upon the orientation of the crystal with respect to the magnetic field. In solution, rapid molecular motion averages the dipolar interaction, generating fluctuating fields which stimulate longitudinal relaxation. The strength of the dipolar interaction is dependent upon internuclear distance, and can cause the cross-relaxation that gives rise to the NOE.

1.1.6 Dipolar coupling

The relation between dipolar coupling, T_1 and NOE is connected through τ_c , the rotational correlation time. Since the size of the dipolar interaction does not depend on τ_c , but its rate of change does, the total power available from the lattice will be constant (i.e. the area underneath the curve of spectral density versus frequency—see Fig. 1.26), while the upper limit of their frequencies will vary with τ_c . Thus if the strength of the fluctuating field, the spectral density function $\mathcal{J}(\omega)$, is plotted against frequency, equal areas are enclosed, but the upper limits vary (see Fig. 1.26). The spectral density is simply the Fourier transform of a correlation function $g(t)$, and a correlation function establishes a correlation between a parameter at time t and at some time later ($t + \tau$), for example it correlates the isotropic motion of a molecule with time, and its rate constant for the decay is in fact the rotational correlation time, τ_c .

We are assuming that the spectral density is constant for $\omega \ll 1/\tau_c$. This then allows predictions to be made about the variation of T_1 , T_2 and W_S with τ_c . For example, as τ_c decreases, ω_0 also decreases, and therefore T_1 increases. At $1/\tau_c \approx \omega_0$ there is a point of inflexion. What is found is shown in Fig. 1.27. For W_0 , W_1 and W_2 relaxation we would predict that in this region at the point of inflexion W_2 would fall off first since it is the sum of two transitions. Without deriving them, the quantitative relaxation rates via dipolar coupling are:

$$W_1^I \propto \frac{3\tau_c}{r^6(1 + \omega_I^2\tau_c^2)} \propto \frac{3\tau_c}{r^6} \quad (\text{under extreme narrowing}) \quad (1.28)$$

$$W_0 \propto \frac{3\tau_c}{r^6(1 + (\omega_I - \omega_S)^2\tau_c^2)} \propto \frac{2\tau_c}{r^6} \quad (\text{under extreme narrowing}) \quad (1.29)$$

$$W_2 \propto \frac{12\tau_c}{r^6(1 + (\omega_I + \omega_S)^2\tau_c^2)} \propto \frac{12\tau_c}{r^6} \quad (\text{under extreme narrowing}) \quad (1.30)$$

Assuming $1/\tau_c \gg \omega_0$ might also be expressed as $\omega_0^2\tau_c^2 \ll 1$, which is called the *extreme narrowing limit*, then the terms above simplify as shown, with the famous $1/r^6$ dependence for NOE. Note, therefore, that for biological macromolecules, this extreme narrowing limit does not hold, and interpretation of the $1/r^6$ dependence is not straightforward.

Although the dipolar interaction, modulated by molecular motion, is the most important relaxation mechanism in solution for protons and other spin- $\frac{1}{2}$ nuclei such as ^{13}C , there are other mechanisms which should be mentioned. Indeed, the overall T_1 is

comprised of many contributing relaxation mechanisms:

$$T_1^{-1} = T_{\text{IDD}}^{-1} + T_{\text{ISR}}^{-1} + T_{\text{IQ}}^{-1} + T_{\text{ISC}}^{-1} + T_{\text{ICSA}}^{-1} \quad (1.31)$$

In addition to dipolar (T_{IDD}) relaxation, there is paramagnetic relaxation, which is a dipolar interaction with the very large magnetic moment of an unpaired electron; and spin-rotation (T_{ISR}) in which there is segmental motion of an aromatic ring, for example. Also, there is quadrupolar relaxation (T_{IQ}), which is due to the coupling of electric field gradients with nuclei possessing a quadrupole moment, scalar coupling relaxation (T_{ISC}),

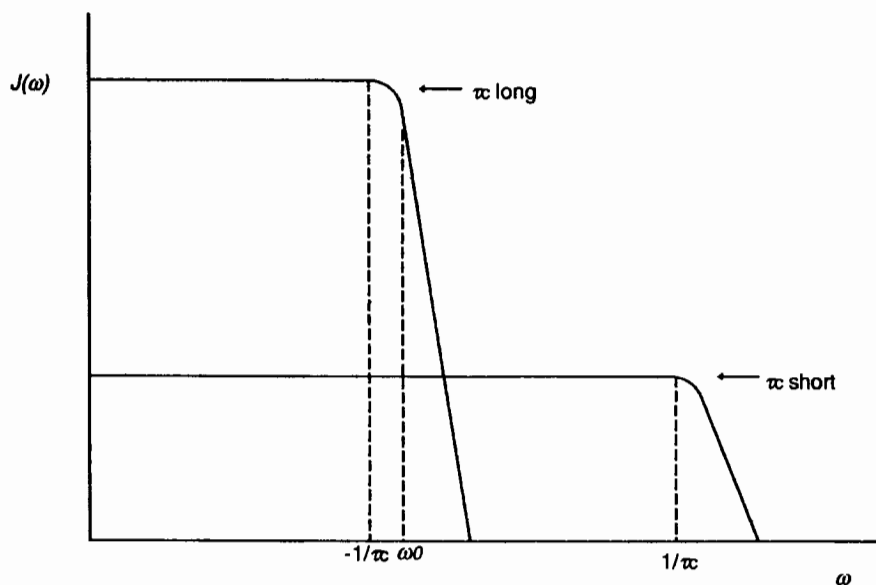


Fig. 1.26 Plot of the spectral density function $J(\omega)$ against frequency (ω).

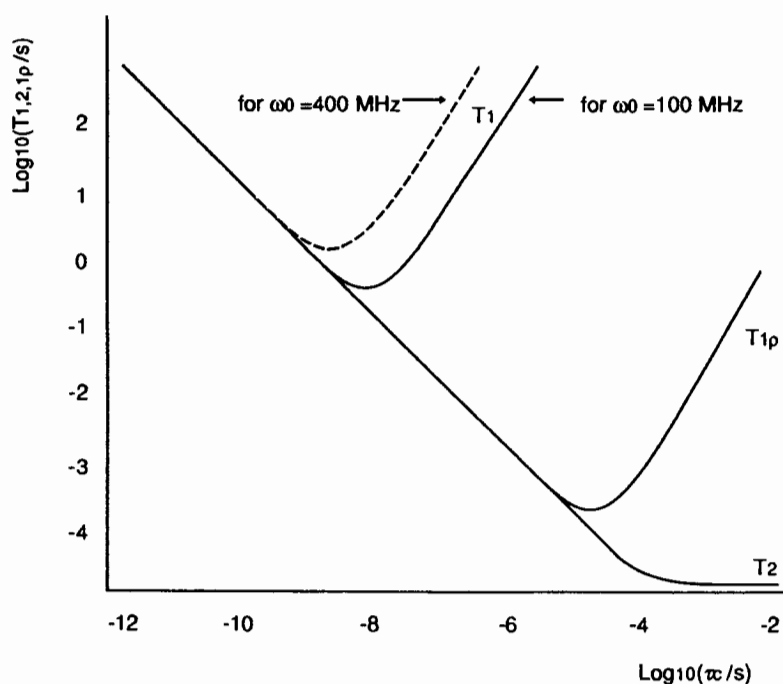


Fig. 1.27 Variations of T_1 and T_2 as a function of τ_c .

which is due to rapidly changing coupling networks; and finally chemical shift anisotropy (T_{ICSA}), which is due to modulation of the chemical shift tensors (σ_{11} , σ_{22} , and σ_{33}) due to molecular motion.

The $^1\text{H}\{^1\text{H}\}$ NOE, which is of prime interest for conformational studies, is $+0.5$ for the extreme motional narrowing situation ($\omega_0^2\tau_c^2 \ll 1$, or $\tau_c \ll \omega_0^{-1}$). For τ_c longer than approximately 1×10^{-9} s it adopts a value of -1.0 (for lower \mathbf{B}_0 fields than 11.7 T, the transition between these limiting values will occur at somewhat longer τ_c), as shown in Fig. 1.28. Note that in a network of like spins contained in a macromolecule with $\tau_c \gg \omega_0^{-1}$, *spin diffusion* by two or several subsequent cross-relaxation steps can greatly influence the observed NOE intensities. For example, with three spins, a two-step pathway for cross-relaxation from spin 1 to spin 2 followed by spin 2 to spin 3, may under certain experimental conditions be more efficient than direct cross-relaxation between spins 1 and 3. The NOE on spin 3 is then no longer a faithful manifestation of the internuclear distance $r_{1,3}$ (see Fig. 1.29).

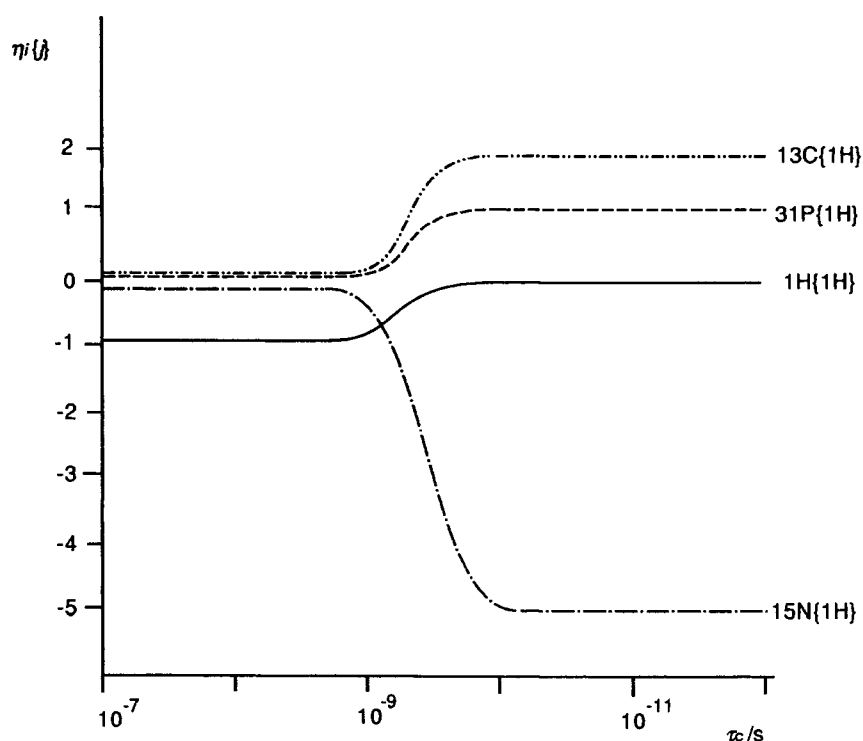


Fig. 1.28 Plots of the maximum NOE versus $\log \tau_c$ for ^1H , ^{13}C , ^{15}N , and ^{31}P interacting with ^1H .

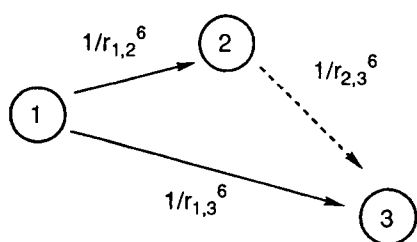


Fig. 1.29 Direct cross-relaxation between two spins 1 and 2, and 1 and 3 spin diffusion pathway from spin 1 via spin 2 to spin 3.

1.1.7 Polarization transfer—the INEPT experiment

In a heteronuclear two-spin AX system, such as ^{13}C — ^1H , the energy level diagram looks very similar to that presented in Fig. 1.24. There are four times the population of the ground state for protons as there are for the carbon-13 nuclei, because the protons have four times the Larmor frequency (because of the ratio of the gyromagnetic ratios, γ) and therefore the energy of the transitions is four times greater. Furthermore, the magnetic moment produced by the protons is four times larger than that due to carbon, so that when a 90° pulse is applied to the protons, the transverse magnetization is 16 times that of carbon. Also, the signal precesses at a rate four times faster for protons, leading to a total signal some 64 times greater than for carbon. In general the signal is proportional to γ^3 . If this is coupled to the fact that ^{13}C has a low natural abundance (introducing another factor of 100), then it is easy to see why the absolute sensitivities of proton and carbon shown in Table 1.2 are of the magnitude given.

There are two ways in which the polarization of one nucleus can be used to enhance another nucleus, usually by no more than γ (it is not possible to recover the full γ^3). In thermodynamic terms, the *spin temperature* (which is another way of expressing the Boltzmann population) of an abundant spin with a high gyromagnetic ratio can be used to ‘warm up’ or increase the spin temperature of a rare spin with a low gyromagnetic ratio. In the liquid state the experiment which is used is the ‘Insensitive Nuclei Enhanced by Polarization Transfer’ or INEPT pulse sequence. In the solid state, as we shall consider in Section 1.2.3, the cross-polarization experiment is used. The basic pulse sequence for the INEPT experiment is shown in Fig. 1.30, where I refers to the source nucleus (e.g. ^1H) and S refers to the destination nucleus (e.g. ^{13}C). Note that the use of the labels I and S is not consistent in the literature, and in the early literature I refers to the ‘insensitive’ nucleus and S the ‘sensitive’ nucleus. In this book we will adopt the convention used in Fig. 1.30, although the reader should always be aware of the context when studying the literature on NMR pulse sequences.

The equilibrium density operator is given by:

$$\sigma_0 \approx I_z + (\gamma_S/\gamma_I)S_z \quad (1.32)$$

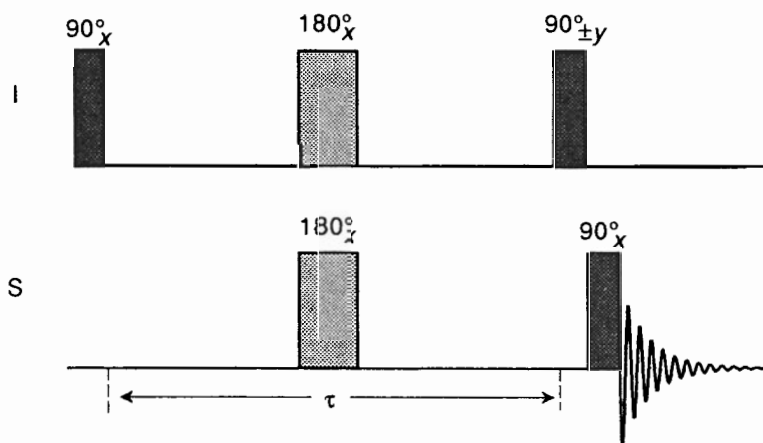


Fig. 1.30 The basic INEPT pulse sequence.

which after the first 90° pulse to the I spins becomes:

$$\sigma_1 \approx -I_y + (\gamma_S/\gamma_I)S_z \quad (1.33)$$

The spins evolve during τ , and the pair of 180° pulses refocuses the chemical shifts, so that the spins undergo the following transformation:

$$-I_y + (\gamma_S/\gamma_I)S_z \xrightarrow{\pi I_x} \xrightarrow{\pi S_x} \xrightarrow{\pi \mathcal{J}_{IS}\tau 2I_z S_z} I_y \cos \pi \mathcal{J}_{IS}\tau - 2I_x S_z \sin \pi \mathcal{J}_{IS}\tau - (\gamma_S/\gamma_I)S_z = \sigma_2 \quad (1.34)$$

Effectively, the 180° I spin pulse removes all chemical shift evolution during the τ period, and the second 180° S spin pulse inverts the S spin labels, ensuring that the I spin vectors continue to precess away from their chemical shift. After the 90° pulse on the I spins (with alternating phase $\pm y$):

$$\sigma_3 \approx I_y \cos \pi \mathcal{J}_{IS}\tau \pm 2I_z S_z \sin \pi \mathcal{J}_{IS}\tau - (\gamma_S/\gamma_I)S_z \quad (1.35)$$

The final 90° pulse on the S spins gives:

$$\sigma_4 \approx I_y \cos \pi \mathcal{J}_{IS}\tau \mp 2I_z S_y \sin \pi \mathcal{J}_{IS}\tau + (\gamma_S/\gamma_I)S_y \quad (1.36)$$

When the two experiments with alternating phase are subtracted, the only term which survives is:

$$\sigma_{\text{obs}} \approx -2I_z S_y \sin \pi \mathcal{J}_{IS}\tau \quad (1.37)$$

If $\tau = 1/2\mathcal{J}_{IS}$, then $\sin \pi \mathcal{J}_{IS}\tau = 1$, and the observed signal is at a maximum. The signal evolves during the detection period, generating antiphase magnetization which is enhanced by a factor of γ_I/γ_S .

The result of this pulse sequence is an antiphase doublet whose intensity is greater than the normal spectrum by a factor of 4 (i.e. by γ_H/γ_C). The result, an example of which is shown in Fig. 1.31, is not perhaps as impressive as one might have predicted. This arises

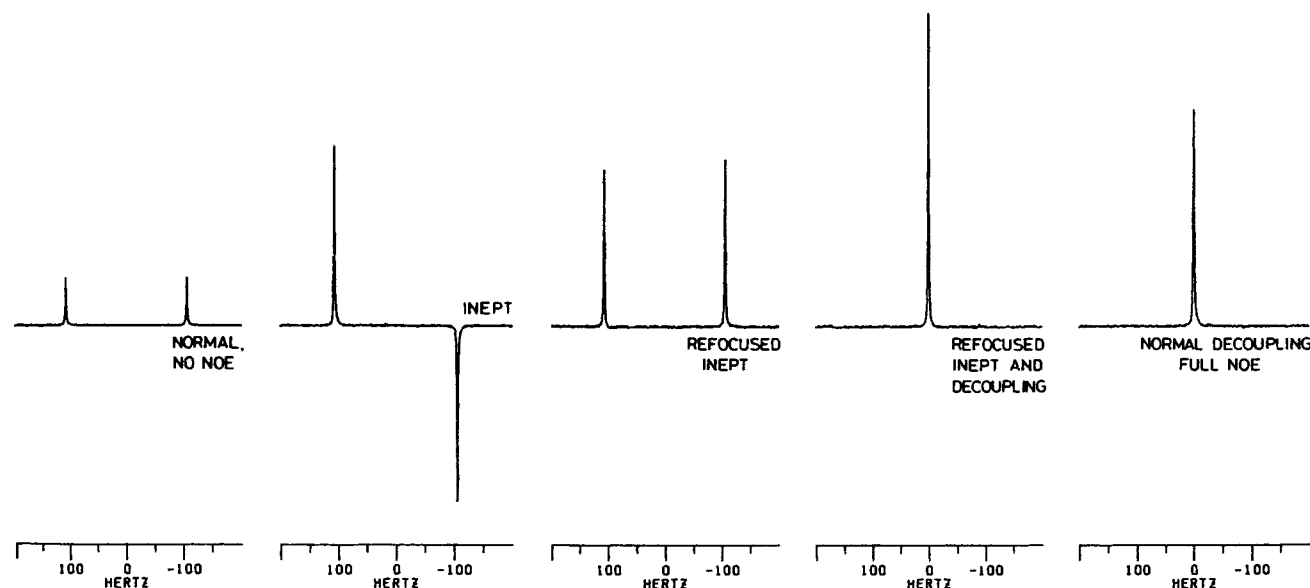


Fig. 1.31 Examples of ^{13}C spectra of chloroform obtained with some variants of the INEPT experiment. (Reprinted from Ref. 7 with permission.)

Table 1.4 Typical ranges of scalar coupling constants

1. $^1\text{H}-^1\text{H}$	Geminal	$^1\text{H}-\text{C}-^1\text{H}$	-12 to -15 Hz
	Vicinal	$^1\text{H}-\text{C}-\text{C}-^1\text{H}$	2-14 Hz
		$^1\text{H}-\text{C}=\text{C}-^1\text{H}$	7 Hz (free rotation average)
		$^1\text{H}-\text{C}\equiv\text{C}-^1\text{H}$	10 Hz (cis) 17 Hz (trans)
	Long range	$^1\text{H}-\text{N}-\text{C}-^1\text{H}$	~ 2 Hz 1-10 Hz 0.5-3 Hz
2. $^1\text{H}-^{13}\text{C}$	Single bond	$^1\text{H}-^{13}\text{C}(\text{sp}^3)$	110-130 Hz
	Long range	$^1\text{H}-\text{C}-^{13}\text{C}$	~ 5 Hz
		$^1\text{H}-\text{C}=\text{C}-^{13}\text{C}$	~ 2 Hz (ethylene)
3. $^1\text{H}-^{15}\text{N}$	Single bond	$^1\text{H}-^{15}\text{N}$	61 Hz (ammonia)
	Long range	$^1\text{H}-^{15}\text{N}$	89-95 Hz (peptides)
		$^1\text{H}-\text{C}-^{15}\text{N}$	15-23 Hz (peptides)
4. $^1\text{H}-^{17}\text{O}$	Single bond	$^1\text{H}-^{17}\text{O}$	17 Hz
	Long range	$^1\text{H}-\text{C}-^{17}\text{O}$	8-10 Hz
5. $^1\text{H}-^{31}\text{P}$		$^1\text{H}-^{31}\text{P}$	170-230 Hz (trivalent ^{31}P) 700-900 Hz (pentavalent ^{31}P)
		$^1\text{H}-\text{O}-^{31}\text{P}$	15-25 Hz
		$^1\text{H}-\text{C}-\text{O}-^{31}\text{P}$	2-20 Hz
6. $^{31}\text{P}-^{31}\text{P}$		$^{31}\text{P}-\text{O}-^{31}\text{P}$	10-30 Hz (pentavalent ^{31}P)
7. $^1\text{H}-^{19}\text{F}$		$^1\text{H}-\text{C}-^{19}\text{F}$	40-50 Hz
		$^1\text{H}-\text{C}-\text{C}-^{19}\text{F}$	5-20 Hz
8. $^1\text{H}-^2\text{H}$		$^1\text{H}-\text{C}-^2\text{H}$	~ -2 Hz
		$^2\text{H}-\text{C}-^2\text{H}$	~ 0.3 Hz

accident. If the nuclei have very different Larmor frequencies, then X, Y are used. Thus, for example, $\text{CHCl}:\text{CHBr}$ is an AB system, but $\text{CHCl}:\text{CFBr}$ is an AX system. ClCH_2CH_3 is an A_2B_3 system, but ClCH_2CF_3 is an A_2X_3 system. When there are more than two well-separated groups of nuclei then the middle letters of the alphabet are used. For example, $^{13}\text{CH}_3\text{F}$ is an AMX_3 system. Examples of calculated AB, AB_2 , and ABX spectra are given in Fig. 1.32. Typical ranges for scalar couplings are given in Table 1.4.

The magnitude of the three-bond (vicinal) coupling constant 3J is a function of the dihedral angle θ , originally derived for $^1\text{H}-\text{C}-\text{C}-^1\text{H}$ coupling from the theoretical calculations of Karplus,²³ and has the form:

$$^3J = A + B \cos \theta + C \cos^2 \theta \quad (1.39)$$

where A, B, and C, are coefficients that depend upon the substituent electronegativity. Karplus relations have been used in various forms for calculating bond angles and

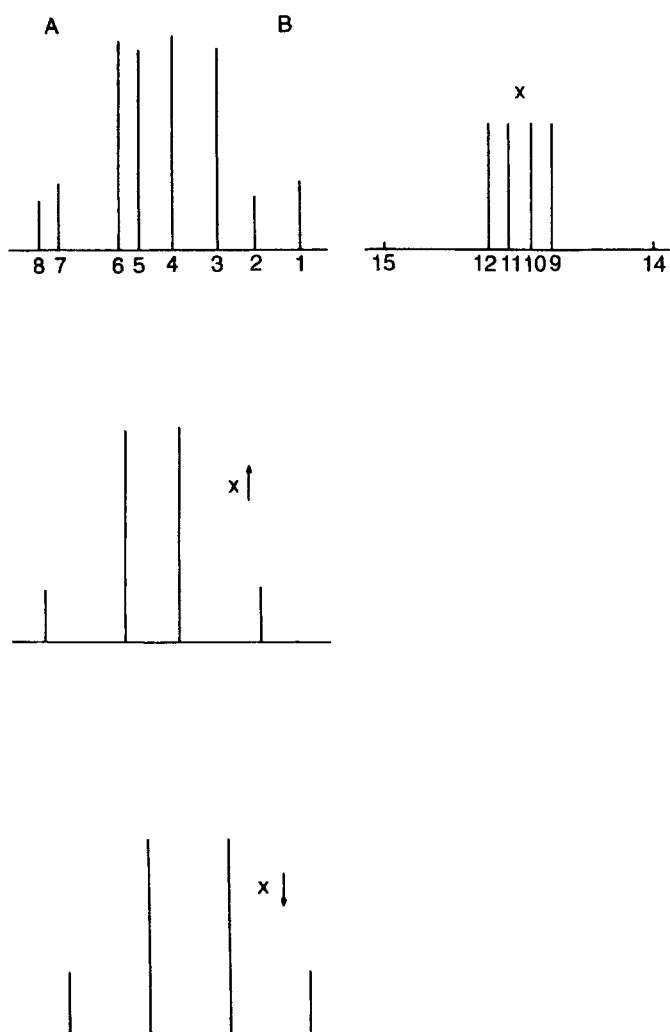
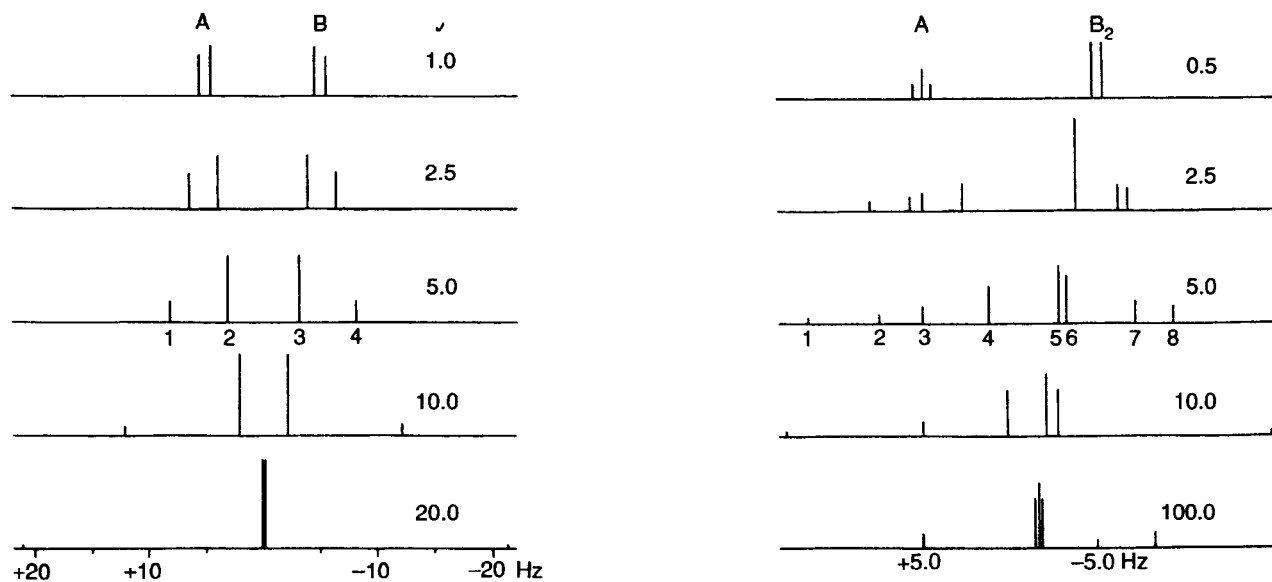


Fig. 1.32 Calculated AB, AB₂, and ABX spectra. (Reprinted from R. J. Abraham, J. Fisher, and P. Loftus, *Introduction to NMR Spectroscopy*, John Wiley & Sons, New York (1988) with permission.)

therefore conformations. However, there are two fundamental assumptions which have to be made: (i) that the molecular fragment involved is rigid, and (ii) the limits of precision are unknown (because it is a truncated cosine function, and the coefficients are obtained semi-empirically). Indeed, Karplus himself wrote that 'anyone who uses this relationship for conformational analysis does so at his peril'.²⁴ With that caveat, it has been used extensively with considerable success (see Fig. 1.33).

So far we have considered scalar coupling without using any particular model to consider what happens to the magnetization under the influence of couplings. In order to do this let us return to the product operator formalism. Spin-spin coupling between two nuclei, 1 and 2, may be described:

$$I_{1x} \xrightarrow{\pi J_{12} t 2 I_{1x} I_{2z}} I_{1x} \cos \pi J_{12} t + 2 I_{1y} I_{1z} \sin \pi J_{12} t \quad (1.40)$$

$$I_{1y} \xrightarrow{\pi J_{12} t 2 I_{1x} I_{2z}} I_{1y} \cos \pi J_{12} t - 2 I_{1x} I_{1z} \sin \pi J_{12} t \quad (1.41)$$

$$2 I_{1x} I_{1z} \xrightarrow{\pi J_{12} t 2 I_{1x} I_{2z}} 2 I_{1x} I_{1z} \cos \pi J_{12} t + I_{1y} \sin \pi J_{12} t \quad (1.42)$$

$$2 I_{1y} I_{1z} \xrightarrow{\pi J_{12} t 2 I_{1x} I_{2z}} 2 I_{1y} I_{1z} \cos \pi J_{12} t - I_{1x} \sin \pi J_{12} t \quad (1.43)$$

These expressions are quite similar to those obtained for the evolution of chemical shifts. However, here for the first time products of two operators are obtained, to which this formalism owes its name. In terms of the vector picture, coupling between spin 1 and spin 2 is shown as two vectors for spin 1, precessing at different angular velocities corresponding to either the α state or the β state of spin 2. The x magnetization of spin 1 is apparently modulated by $\cos \pi J t$, as is shown in the first part of Equation (1.40). In addition there is a magnetization along the y axis, which is described by $I_{1y}(I_2^\alpha - I_2^\beta)$ (the y magnetization of spin 1 points to $+y$ for the case where spin 2 is in the α state, and to $-y$ for spin 2 in the β state). This y magnetization is not observable, thus, in the macroscopic sense, it is not really a magnetization, since the positive and negative components cancel

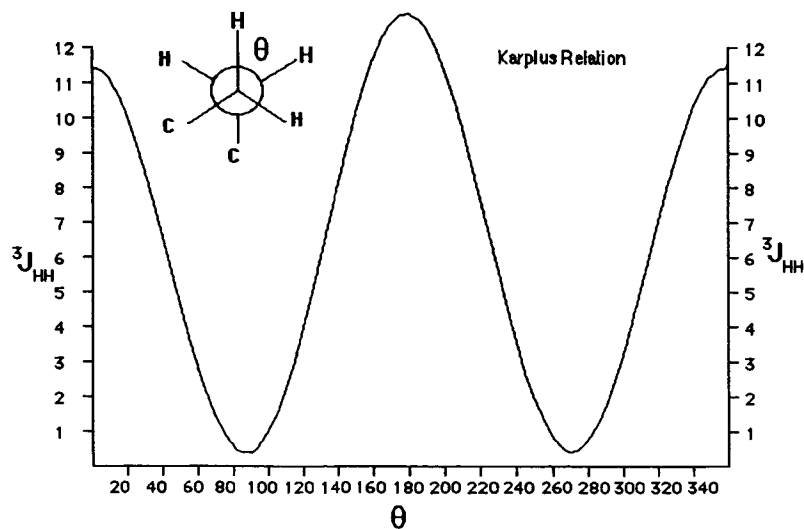


Fig. 1.33 Plot of the three-bond coupling constant 3J versus the dihedral angle θ .

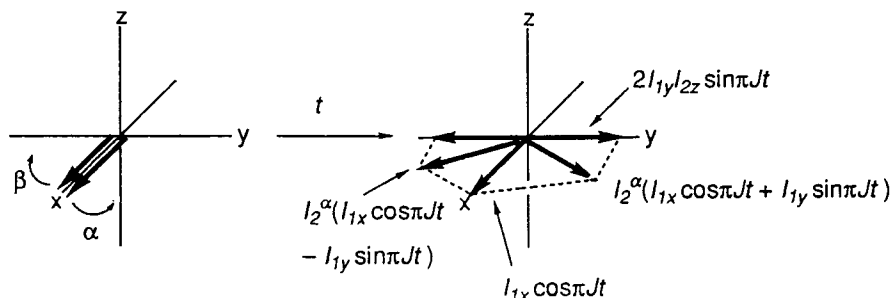


Fig. 1.34 Vectorial representation of the product operator of coupled spins.

exactly. The difference in populations of the α and β levels ($I^\alpha - I^\beta$) is given by $2I_z$. Hence, $I_{1y}(I_2^\alpha - I_2^\beta)$ is identical to $2I_{1y}I_{1z}$, which is obviously modulated by $\sin \pi J t$ (see Fig. 1.34).

In contrast to the evolution under chemical shift and/or pulses, the evolution of coupling 'creates' or 'annihilates' operators: $I_{1x} \rightarrow 2I_{1y}I_{2z}$ and $2I_{1x}I_{2z} \rightarrow I_{1y}$. Only coupling and not chemical shift can bring other nuclei into the picture, which is one of the salient features for coherence transfer, since coherence can be transferred only when a second spin is involved in the product operator. Equations (1.40) and (1.41) correspond to the conversion of in-phase magnetization into orthogonal antiphase magnetization, and, starting with antiphase magnetization. Equations (1.42) and (1.43) correspond to the evolution under scalar coupling of in-phase magnetization. This has important consequences for the appearances of multiplets in two-dimensional spectra, which we will consider in Chapter 2.

1.1.9 Populations and coherences

Coherence is a relationship between two states across a single nuclear transition, or multiple states for multiple transitions. A good example of the difference between magnetization and coherence is to consider the case where an NMR transition has been saturated compared with one which has just undergone a 90° pulse. For the saturated transition, there will be no magnetization at all. For the transition which has undergone a 90° pulse, there will be xy components precessing together with the same phase, which they derived from the pulse. In the saturated sample the nuclei are precessing incoherently, and in experiencing a pulse they are precessing with *phase coherence*. For a coherence across one transition this is called a *single-quantum coherence*. When more than one level is involved, then the relationship between the levels is such that *multiple-quantum coherences* may be transferred. However, only single-quantum coherences may be detected by NMR. Thus *coherence* is a generalization of *magnetization*, and in fact corresponds to transverse magnetization. This is in contrast to *polarizations*, which correspond to longitudinal magnetization.

Thus, application of a high-frequency pulse to the z magnetization (spin state I_z) which is initially at its Boltzmann equilibrium produces transverse magnetization (state I_x). During this state the so-called coherence evolves during the detection period time t . This variation of intensity with time can be observed by detection of an induced signal in the receiver coil (I_x, I_y are associated with transverse magnetization). In other words, coherences produced by product operators are displayed at characteristic frequencies.

This concept of the coherence is important. In contrast to populations, which are the occupation of states in the energy level scheme, coherences describe transitions among different energy levels. These are characterized by Δm_I for the quantum number m_I . This change Δm_I is the coherence order p , which is essential for describing phase cycles. Although in general many of the possible coherences occur under the influence of pulses in a pulse sequence, only a few are associated with observable magnetizations, i.e. $\Delta m_I = \pm 1$ (the selection rule for NMR). Of these single-quantum coherences, only a few are detectable under weak coupling conditions (see Fig. 1.35): those in which the state of exactly one spin is changed (i.e. product operators with only one transverse operator).

We can assume that the state of all the spins in the sample (the 'spin ensemble') is a superposition of (i) the populations of the states and (ii) the coherences between the states. These coherences are indexed by their order p . Populations are the same as coherences between a state and itself (e.g. populations are a special type of zero-quantum coherence). The only coherences which induce an observable NMR signal are the (-1) -quantum coherences. Populations are long-lived and do not oscillate; coherences are short-lived and oscillate, and we can refer to coherences + populations as 'normal modes'. The normal modes for a single spin- $\frac{1}{2}$ consist of two energy levels and four normal modes (see Fig. 1.36).

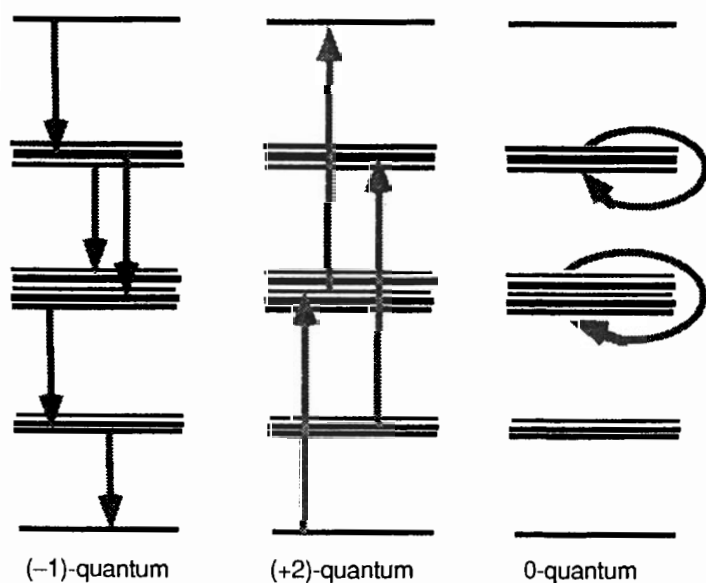


Fig. 1.35 Single-, double- and zero-quantum coherences.

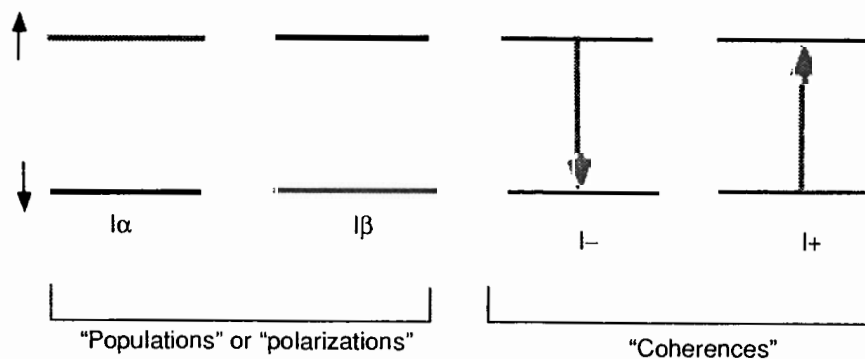


Fig. 1.36 The normal modes for a single spin- $\frac{1}{2}$.

The single-quantum coherences can be represented in terms of product operators or vectors, as well as energy levels, as illustrated in Fig. 1.37(a). However, other coherences are also possible in two-spin (or more) systems, and these give rise to zero-quantum and double-quantum coherences, as shown in Fig. 1.37(b). Two-spin coherence terms consist of superpositions of $p=0$ and $p=\pm 2$ quantum coherence. These give rise to the products of two operators which are not observable in the NMR experiment.

1.1.10 Chemical shifts

The chemical shift is one of the most basic parameters of NMR, and is generally defined as δ in parts per million (ppm):

$$\delta = \frac{\omega - \omega_0}{\omega_0} \times 10^6 \quad (1.44)$$

where ω_0 is the Larmor frequency in Hz, and ω is the resonant frequency of the line of

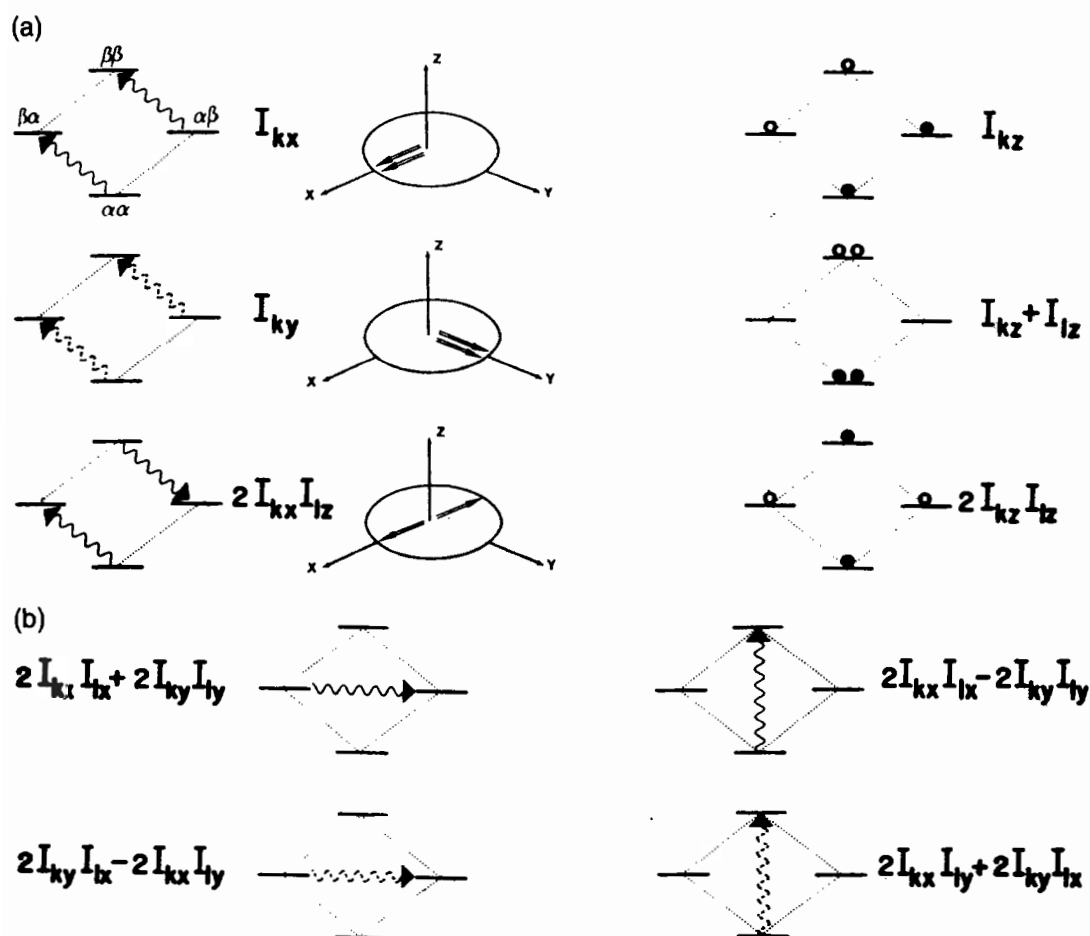


Fig. 1.37 Graphic representation of product operators representing: (a) single-quantum magnetization and longitudinal magnetization; (b) pure zero- and double-quantum coherence, in a two-spin system with $I = \frac{1}{2}$, and each spin operator referred to generally as I_k or I_l . The oscillating x and y magnetization components are represented by wavy lines (with dashed lines for y components) in the energy level diagram, or by the customary vectors in the xy plane of the rotating frame. Populations are represented by open circles for depleted states and filled circles for more populated states (compared with the demagnetized saturated state). (Reprinted from Ref. 19 with permission.)

interest, and note that we have used $\Omega = \omega - \omega_0$ in Section 1.1.3. The origin of the chemical shift is that the moving electric charges of the electron cloud around a nucleus induce a local magnetic field which opposes the applied field. Thus the effective field at the nucleus is:

$$\mathbf{B}_{\text{eff}} = \mathbf{B}_0(1 - \sigma) \quad (1.45)$$

The nucleus is said to be *shielded*, and the extent of the shielding is given by the shielding constant, also called the chemical shift tensor, σ . This is directly related to the electron density ρ at a distance r from the nucleus by Lamb's equation:

$$\sigma = \frac{4\pi e^2}{3mc^2} \int_{-\infty}^{\infty} r\rho(r) dr \quad (1.46)$$

There are three principal components of the shift tensor, σ_{11} , σ_{22} , and σ_{33} , and the isotropic shift tensor σ_{iso} is given by:

$$\sigma_{\text{iso}} = \frac{1}{3}(\sigma_{11} + \sigma_{22} + \sigma_{33}) \quad (1.47)$$

The shift tensor σ is related to the Larmor frequency, ω_0 , as follows:

$$\omega_0 = \frac{\gamma}{2\pi} \mathbf{B}_0(1 - \sigma) \quad (1.48)$$

and to chemical shift:

$$\delta = 10^6 (\sigma_{\text{ref}} - \sigma_{\text{sample}}) \quad (1.49)$$

The chemical-shift anisotropy is illustrated in Fig. 1.38, where the different local magnetic fields of the nuclei in an anisotropic C–H bond is shown as a function of orientation with respect to the applied field, \mathbf{B}_0 . These differences are reflected in the chemical shift tensor. Typical values for chemical shifts of nuclei commonly encountered in biology are shown in Fig. 1.39.

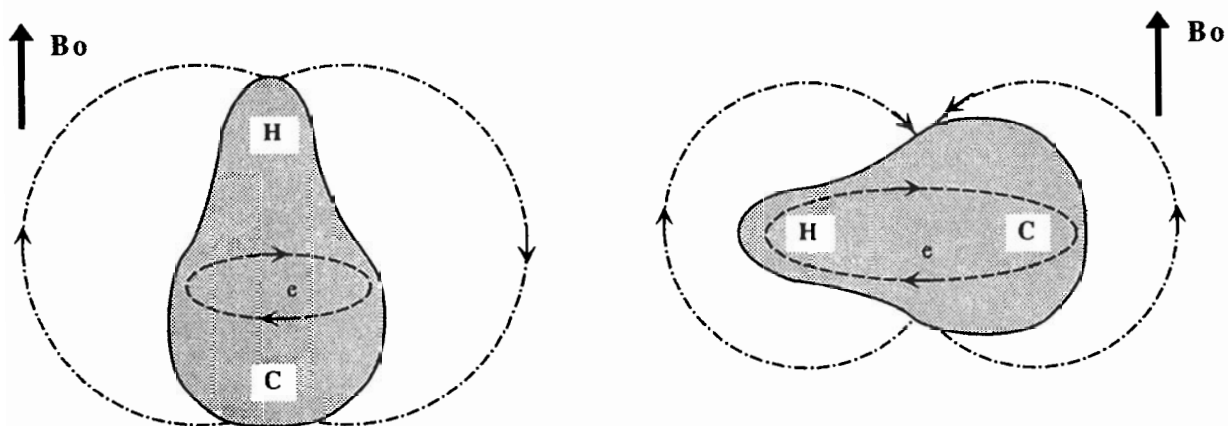


Fig. 1.38 Origins of chemical-shift anisotropy in a C–H bond. The circulation of the electrons in a plane perpendicular to the bond describes a smaller area than circulation in a plane containing the bond. (Redrawn from ref. 12 with permission.)

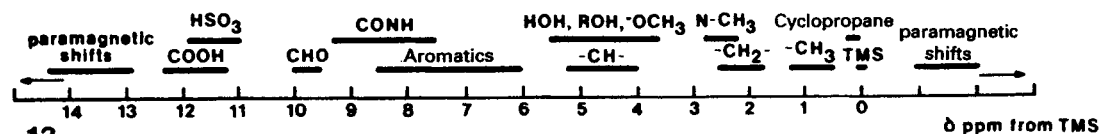
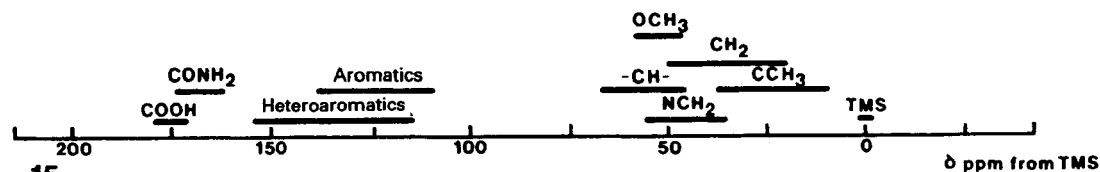
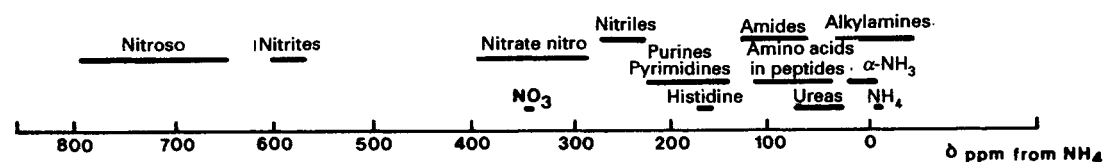
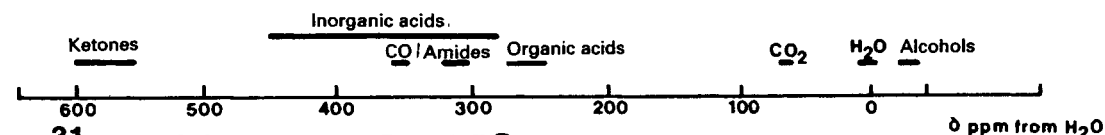
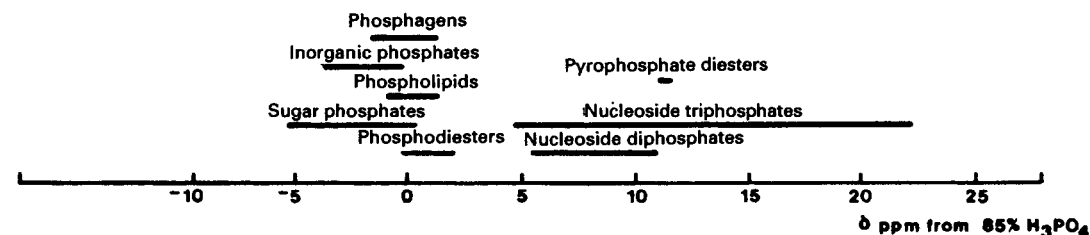
^1H RESONANCE SHIFTS **^{13}C RESONANCE SHIFTS** **^{15}N RESONANCE SHIFTS** **^{17}O RESONANCE SHIFTS** **^{31}P RESONANCE SHIFTS**

Fig. 1.39 Ranges of chemical shifts for ^1H , ^{13}C , ^{15}N , ^{17}O , and ^{31}P . (Reprinted from Ref. 12 with permission.)

1.2 SOLID-STATE NMR

A number of excellent texts are available in the field of solid-state NMR,^{6,25-28} although many are rather dated, somewhat mathematical, and none deal with biological solids.

1.2.1 The source of broad lines in solid samples

Figure 1.40(a) shows the ^{13}C spectrum of crystalline glycine without ^1H decoupling. Given the quality of this spectrum, one might be forgiven for thinking that NMR of solids is not very helpful for obtaining structural information. However, there are a number of methods for obtaining narrow lines in solid-state spectra.

Recall that in its simplest form, the relationship between the wave function Ψ of a quantized particle (i.e. a nucleus) and the energy is given by the Schrödinger equation:

$$\mathcal{H}\Psi = E\Psi \quad (1.50)$$

\mathcal{H} is the Hamiltonian operator, which for a heteronuclear two-spin system in a magnetic field includes a number of contributing Hamiltonians which until now we have expressed in terms of Cartesian product operators. These operators describe all the interactions which the spins experience. In order to understand solid-state NMR, it is more convenient to consider these Hamiltonians:

$$\mathcal{H}_{\text{TOTAL}} = \mathcal{H}_Z + \mathcal{H}_\delta(\theta) + \mathcal{H}_{\text{II}}(\theta) + \mathcal{H}_{\text{SS}}(\theta) + \mathcal{H}_{\text{IS}}(\theta) \quad (1.51)$$

Consider each Hamiltonian in turn:

The Zeeman Hamiltonian, \mathcal{H}_Z

$$\mathcal{H}_Z = \gamma\hbar\mathbf{B}_0 I_z \quad \text{where} \quad \omega_0 = \gamma\mathbf{B}_0 \quad (1.52)$$

The chemical-shift Hamiltonian, $\mathcal{H}_\delta(\theta)$

$$\mathcal{H}_\delta(\theta) = \sigma_i \omega_0 I_z + \frac{1}{2}(3 \cos^2 \theta - 1)(\sigma_{33} - \sigma_i) \omega_0 I_z \quad (1.53)$$

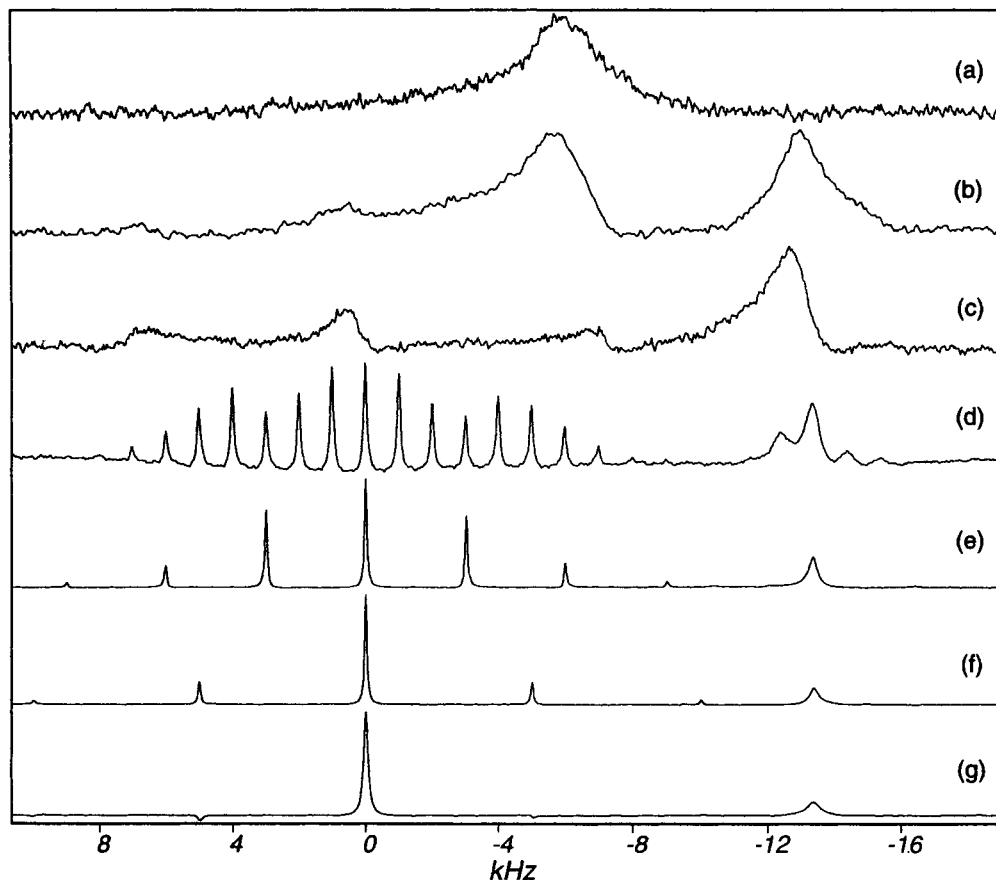


Fig. 1.40 ^{13}C NMR spectra of crystalline glycine: (a) without proton decoupling; (b) with proton decoupling; (c) with proton decoupling and cross-polarization; (d) CPMAS ($\nu_R = 1$ kHz); (e) CPMAS ($\nu_R = 3$ kHz); (f) CPMAS ($\nu_R = 5$ kHz); (g) CPMAS ($\nu_R = 5$ kHz) plus sideband suppression (TOSS).

The homonuclear spin coupling Hamiltonian, $\mathcal{H}_{\text{II}}(\theta)$

$$\begin{aligned} \mathcal{H}_{\text{II}}(\theta) = & \mathcal{J} \mathbf{I}_1 \cdot \mathbf{I}_2 - \frac{1}{2} \cos \theta (\mathbf{D}_{x'y'} - \mathbf{D}_{y'x'}) (I_{1x} I_{2y} - I_{1y} I_{2x}) \\ & + \frac{1}{2} (3 \cos^2 \theta - 1) \frac{1}{2} (\mathbf{D}_{z'z'} - \mathcal{J}) (3 I_{1z} I_{2z} - \mathbf{I}_1 \cdot \mathbf{I}_2) \end{aligned} \quad (1.54)$$

The heteronuclear spin coupling Hamiltonian, $\mathcal{H}_{\text{IS}}(\theta)$

$$\mathcal{H}_{\text{IS}}(\theta) = \mathcal{J} I_z S_z + \frac{3}{2} (3 \cos^2 \theta - 1) \frac{1}{2} (\mathbf{D}_{z'z'} - \mathcal{J}) I_z S_z \quad (1.55)$$

In all these expressions, $\mathbf{D}_{x'y',z'}$ are the principal components of the dipolar coupling tensor in the sample rotation frame, and θ is the angle between the applied magnetic field and the axis of rotation for a pair of dipolar coupled spins (see Fig. 1.41). Note that these Hamiltonians are all time-independent, which means that they are effectively ‘stroboscopic’, sampling the interactions at one full sample rotation cycle.

1.2.2 Magic-angle spinning

In solution, rapid isotropic motion averages all the θ -dependent terms of the interaction Hamiltonians to zero, leaving the total Hamiltonian as:

$$\mathcal{H}_{\text{TOTAL}} = \mathcal{H}_Z + \mathcal{H}_\delta + \mathcal{H}_{\text{IS}}(\mathcal{J}) \quad (1.56)$$

which is the familiar Hamiltonian that dominates solution-state pulsed NMR. Note that the dipolar coupling D falls to zero.

When the rather interesting condition that $(3 \cos^2 \theta - 1) = 0$ is met, or $\theta = 54^\circ 44'$, the so-called ‘magic angle’, all the terms in the interaction Hamiltonians containing $(3 \cos^2 \theta - 1)$ tend to zero. In other words,

$$\mathcal{H}_{\text{TOTAL}} = \mathcal{H}_Z + \mathcal{H}_\delta + \mathcal{H}_{\text{II}}(\theta) + \mathcal{H}_{\text{SS}}(\theta) + \mathcal{H}_{\text{IS}}(\mathcal{J}) \quad (1.57)$$

In practical terms this means spinning the sample at an angle of $54^\circ 44'$ with respect to \mathbf{B}_0 , which is known as magic-angle spinning (MAS), as shown in Fig. 1.42.

The effect of MAS on the spectrum of glycine (in conjunction with cross-polarization—see Section 1.2.3) is illustrated in Fig. 1.40(d–f). Also shown is the use of sideband suppression pulse sequences such as T_OTal Sideband Suppression (TOSS),²⁹ which removes the rotational sidebands without enhancing the intensity of the centre band (as opposed to using higher spinning rate MAS, which does enhance the centre band intensity).

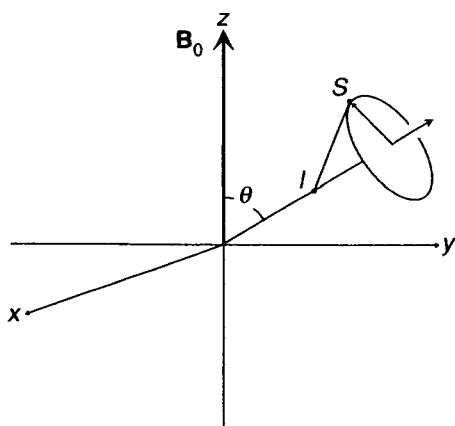


Fig. 1.41 A diagram showing the angle θ between the applied magnetic field \mathbf{B}_0 and the sample rotation axis, for an isolated pair of dipolar coupled spins, IS .

1.2.3 Cross-polarization

Another trick for obtaining narrow lines in solid-state NMR spectra is to use ‘dilute spins’. An example of this is the use of natural abundance ^{13}C , where the odds of there being a ^{13}C within interaction distance of another ^{13}C are so low that the term $\mathcal{H}_{\text{SS}}(\theta)$ can be neglected:

$$\mathcal{H}_{\text{TOTAL}} = \mathcal{H}_Z + \mathcal{H}_\delta + \mathcal{H}_{\text{IH}}(\theta) + \mathcal{H}_{\text{IS}}(\mathcal{J}) \quad (1.58)$$

If high-power decoupling is applied to the I spins, then the total Hamiltonian simplifies even further:

$$\mathcal{H}_{\text{TOTAL}} = \mathcal{H}_Z + \mathcal{H}_\delta \quad (1.59)$$

Enhancement of sensitivity for the dilute spins can be achieved through a technique called *cross-polarization*. This technique relies on polarization transfer from the abundant spins, for example ^1H , to the rare spins such as ^{13}C , through matching the \mathbf{B}_1 RF fields of the ^1H s and the ^{13}C s. It is analogous to the solution-state INEPT experiment (see Section 1.1.7). This is known as fulfilling the *Hartmann–Hahn condition*, which is as follows:

$$\gamma_{\text{H}}\mathbf{B}_{\text{IH}} = \gamma_{\text{C}}\mathbf{B}_{\text{IC}} \quad (1.60)$$

where \mathbf{B}_{IH} and \mathbf{B}_{IC} are known as the RF *spin locking* fields. Since $\gamma_{\text{H}}/\gamma_{\text{C}} = 4$, then $\mathbf{B}_{\text{IH}} = 4\mathbf{B}_{\text{IC}}$, and the sensitivity of the ^{13}C spins are enhanced by the ^1H spins by a factor of 4.

The pulse sequence for cross-polarization (CP) is shown in Fig. 1.43. In the first step,

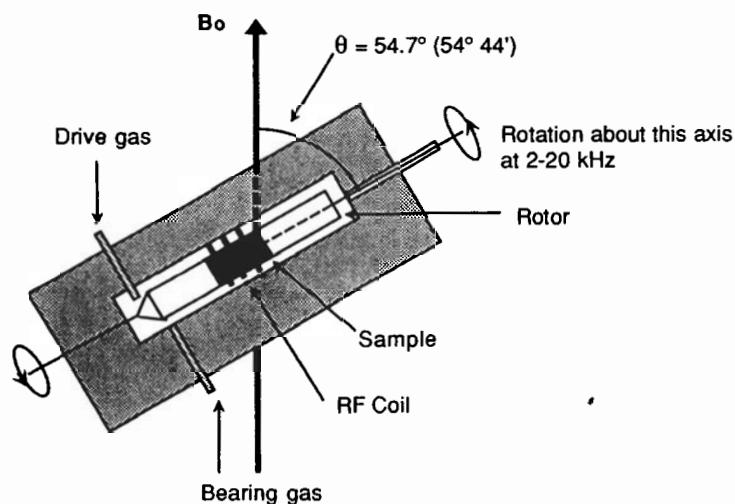


Fig. 1.42 Diagrammatic representation of the magic-angle spinning experiment.

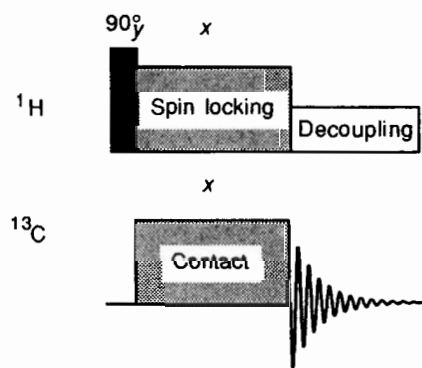


Fig. 1.43 Pulse sequence for cross-polarization (CP).

the proton magnetization is rotated through 90° to the x axis and then held there by a ‘spin locking’ pulse (see Fig. 1.44). The proton spins are kept locked for a time period t , known as the *contact time*. During this time period, a strong on-resonance pulse is applied to the ^{13}C spins which also orient along the x axis. If the Hartmann–Hahn condition is met, and the two spin locking fields are matched, the net carbon magnetization will be enhanced by the proton reservoir. Since the ^{13}C spins are very dilute in the system, they will adopt the more favourable spin distribution of the proton system, while the total proton magnetization will be affected minimally. After the carbon magnetization has built up during the contact time, the carbon field is switched off, and the FID recorded. The proton field is kept on for high-power decoupling. One of the important consequences of this pulse sequence is that the carbon magnetization which yields an FID does not depend on the regrowth of the carbon magnetization in between scans, but arises entirely from contact with the proton spins. This means that the intensity of the carbon spectrum effectively depends on the relaxation of the proton spin system. This relaxation time, for protons spin locked in the rotating frame, is a rather special quantity denoted $T_{1\rho}$. The great advantage of this is that, generally, the ^1H relaxation times are much shorter than the ^{13}C relaxation times, so that successive scans may be recycled much faster than for normal ^{13}C acquisitions, yielding better signal-to-noise in a given time period.

When CP is combined MAS, high-resolution spectra, comparable to solution state spectra are obtained. For example, in the ^{13}C NMR spectrum of glycine shown in Fig. 1.40, CP–MAS leads to narrow lines, and when combined with sideband suppression pulse sequences, such as TOSS, give rise to high-resolution spectra.

1.2.4 Shielding anisotropy

By appropriate choice of a coordinate system, the chemical shift tensor σ , which is a three by three matrix, or second-rank tensor, may be converted to three principal elements, σ_{11} , σ_{22} , and σ_{33} , which serve to characterize the three-dimensional nature of shielding (see Section 1.1.10). From these elements we may define the *shielding anisotropy* $\Delta\sigma$ and the *shielding asymmetry parameter* η as follows:

$$\Delta\sigma = \sigma_{33} - \frac{1}{2}(\sigma_{11} + \sigma_{22}) \quad (1.61)$$

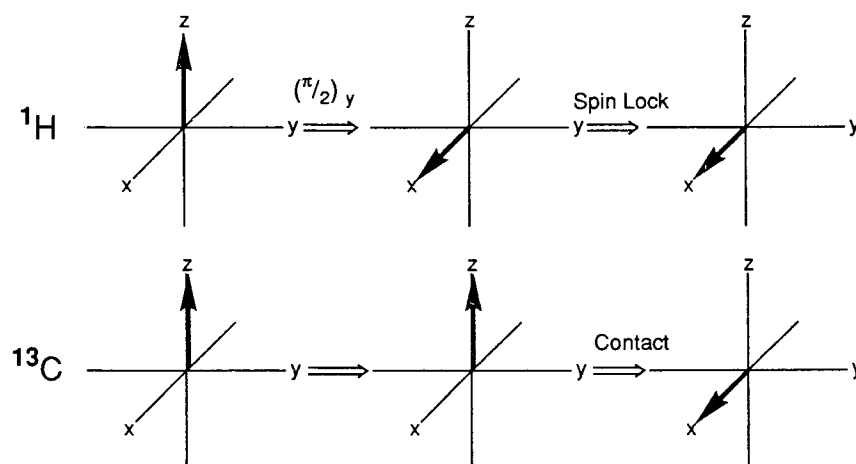


Fig. 1.44 Vector representation for cross-polarization (CP).

$$\eta = \frac{\sigma_{22} - \sigma_{11}}{\sigma_{33} - \sigma_{\text{iso}}} \quad (1.62)$$

The principal elements of the shift tensor can be obtained by rotational sideband intensity analysis.³⁰ The parameter $\Delta\sigma$ provides an estimate of the departure from spherical symmetry of the electrons around the nucleus.

Recall that in solution the isotropic molecular motion averages the shift anisotropy, $\sigma_{\text{iso}} = \frac{1}{3}(\sigma_{11} + \sigma_{22} + \sigma_{33})$. In the solid state, the chemical-shift anisotropy will be manifested according to the state of the sample:

- In a single crystal in a fixed orientation to the magnetic field, a single sharp line will be observed for each magnetically unique orientation of a particular nucleus with respect to the field direction, and the positions of these lines will change as the orientation of the crystal is changed;
- For a powdered sample, signals as in (a) will arise from each random crystallite orientation and a broad line will result, the shape of which will depend on the principal elements of the shielding tensor (see Fig. 1.45).

In case (a) in Fig. 1.46 given below, the principal tensor elements have the values indicated. Another common situation is illustrated in Fig. 1.46(b), in which two of the

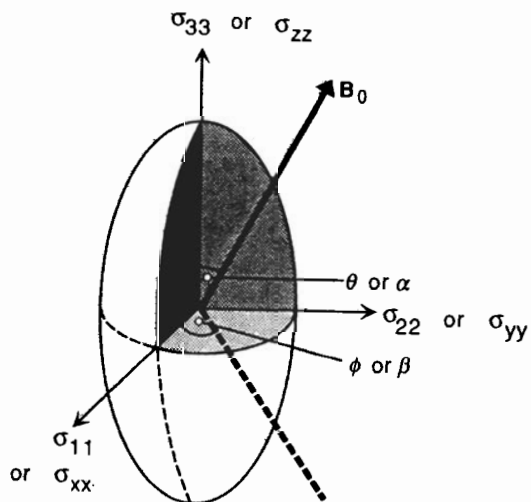


Fig. 1.45 The chemical shielding ellipsoid, which is used to indicate that different orientations of the magnetic field relative to the molecular framework result in different resonance positions for the same chemical species.

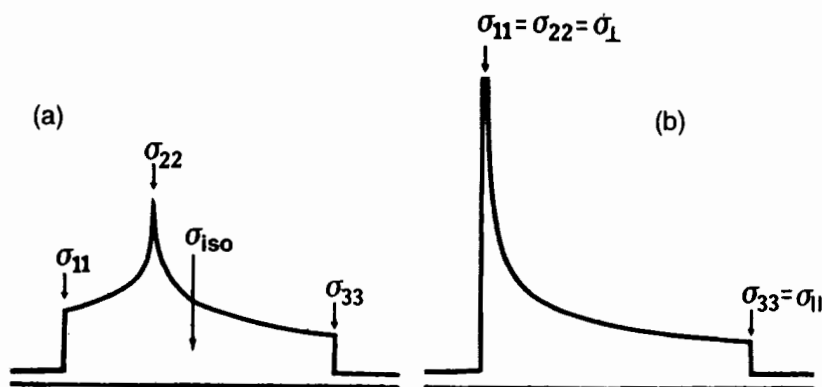


Fig. 1.46 Schematic representation of theoretical powder line shapes for the chemical-shift tensor, (a) asymmetric shift anisotropy, (b) axially symmetric shift anisotropy. (Reprinted from Ref. 28 with permission.)

elements are identical, and the shielding pattern is called *axially symmetric*. The shielding element of the unique axis is described as σ_{\parallel} and the other two as σ_{\perp} . Such a situation can arise either by chance, or by the presence of molecular motion which partially averages the shift anisotropy.

1.2.5 Quadrupolar effects

For quadrupolar nuclei, such as ^2H , the interaction Hamiltonian is given by:

$$\mathcal{H}_Q = \frac{eQ}{2I(2I-1)} h\mathbf{I} \cdot \mathbf{V} \cdot \mathbf{I} \quad (1.63)$$

where \mathbf{V} is the electric field gradient tensor at the nuclear site, eQ is the quadrupole moment for a single spin with nuclear spin quantum number, I and \mathbf{I} is the angular momentum operator (I_x, I_y, I_z). If it is assumed that the Zeeman interaction is much larger than the quadrupolar interaction, the so-called high-field approximation, which is reasonable for a nucleus such as ^2H , then the energy shifts due to the quadrupolar interaction for a single nucleus may be obtained as follows:

$$\Delta E_Q = 3/8 \left(\frac{e^2qQ}{h} \right) (3 \cos^2 \theta - 1) \quad (1.64)$$

where ΔE_Q is the energy shift due to the quadrupolar interaction, and θ is the angle between the principal component of the electric field gradient tensor (eq) and the applied magnetic field vector.

The energy level diagram for the combined Zeeman and quadrupolar interactions for a spin-1 nucleus is shown in Fig. 1.47. Note that $m = -1$ and $m = +1$ levels are affected equally and in the same direction by the quadrupolar interaction. The allowed transitions are shown, and the spectrum for a single spin-1 nucleus interacting with an axially symmetric field gradient consists of a doublet with peak separations given by:

$$\Delta\nu = 3/4 \left(\frac{e^2qQ}{h} \right) (3 \cos^2 \theta - 1) \quad (1.65)$$

where (e^2qQ) is the *quadrupole coupling constant*, θ is the Euler angle between the principal axis system and the laboratory frame.

For a polycrystalline material, the energy is averaged over all possible crystal orientations, yielding the spectrum shown, the characteristic *Pake doublet* (see Fig. 1.48).

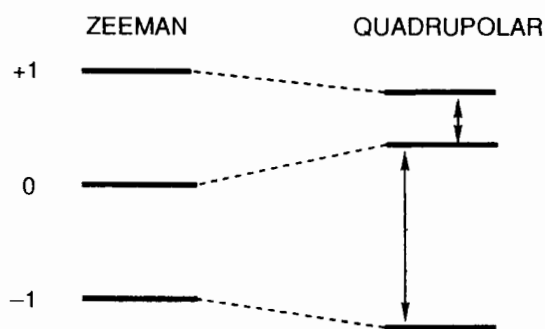


Fig. 1.47 Energy level diagram for the combined Zeeman and quadrupolar interactions for a spin-1 nucleus.

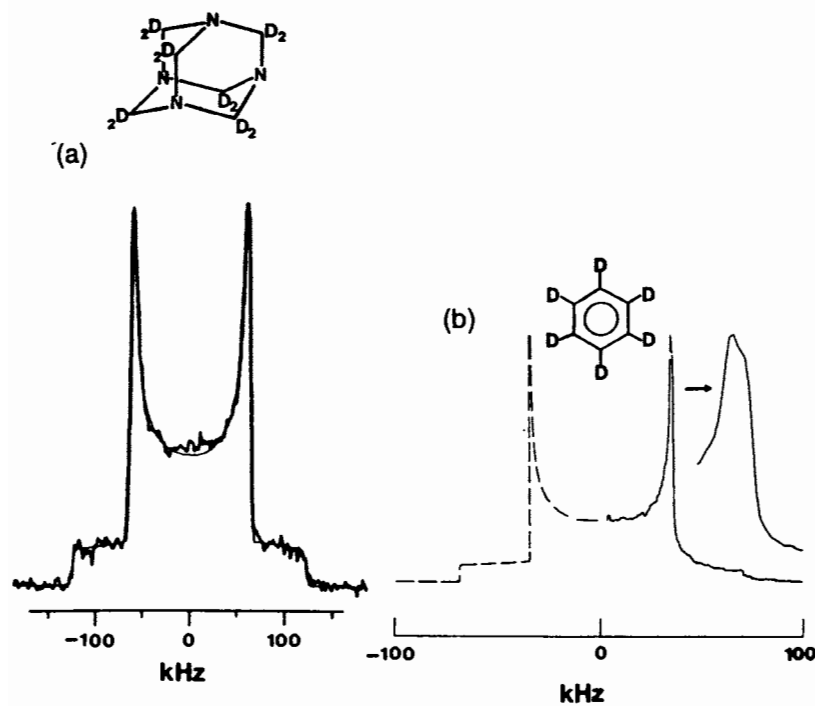
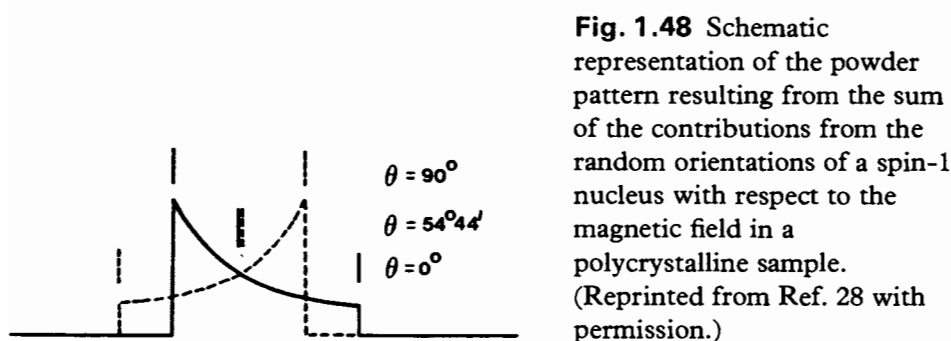
The 'steps' at the wings of the spectrum correspond to $\theta = 0^\circ$, and the central pair of peaks to $\theta = 90^\circ$ and the mid-point to $\theta = 54^\circ 44'$ where the two peaks from the quadrupolar splitting coalesce, and the quadrupolar interaction, in effect, vanishes. The total spectrum is the summation of two axially symmetric distributions reversed in sign and corresponding to the two lines in the doublet. The dashed curves indicate the envelopes from the separate contributions of each peak. For a rigid deuteron, the separation of the central doublet is:

$$\Delta\nu_1 = 3/4 \left(\frac{e^2 q Q}{h} \right) \quad (1.66)$$

and that of the outermost steps is:

$$\Delta\nu_2 = 3/2 \left(\frac{e^2 q Q}{h} \right) \quad (1.67)$$

An example of this is shown in Fig. 1.49.



1.3 KINETICS

1.3.1 The NMR timescale

The NMR timescale is defined by the nuclear precession frequency, and kinetic processes or molecular motions that occur on this time scale are reflected directly in the chemical shift (δ), scalar coupling (\mathcal{J}), and relaxation parameters (T_1 and T_2). For molecules in solution, there are many situations in which groups of nuclei exchange reversibly between two or more different environments. This exchange may reflect conformational flexibility, chemical reactions, formation of intermolecular complexes, or other events. The timescales in relation to the motional correlation time τ_c which are probed by NMR are summarized in Table 1.5.

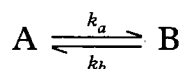
Depending on the nature of the exchange process, the different environments undergoing exchange will be characterized by different values of the NMR parameters: chemical shift, coupling constant, and relaxation rates. If the measured variable is chemical shift, with exchange occurring between two environments characterized by shifts δ_A and δ_B , *slow exchange* occurs if the exchange rate $k \ll |\delta_A - \delta_B|$, *intermediate exchange* if $k \approx |\delta_A - \delta_B|$, and *fast exchange* if $k \gg |\delta_A - \delta_B|$. Similar expressions can be derived for the other NMR parameters, and is expressed in terms of lifetimes, $\tau (= 1/k)$ (see Table 1.6).

Note that the three parameters define quite different, although partially overlapping, timescales. For example, chemical-shift differences are of the order of 10–500 Hz (at ^1H frequencies of 200–400 MHz), so that fast exchange with respect to chemical shift will be observed for systems in which the lifetime is less than a few milliseconds. Since the chemical shift is field dependent, so is the chemical-shift difference between two environments, and populations of nuclei that appear to be in fast exchange on low-field spectrometers can sometimes be found in the intermediate or even slow exchange region on high-field spectrometers. For protons, typical differences in coupling constants are of the order of 10 Hz, and these coupling constants will be averaged even if the lifetime is as long as ≈ 100 ms. For the much larger coupling constants seen for other nuclei (e.g. ^{15}N — ^1H) the timescale is comparable to the chemical-shift scale. Much shorter lifetimes, about 10^{-4} s, may be required for relaxation time averaging, since relaxation times of 10^{-3} s can often be observed, especially with macromolecular systems.

Whether a system is in the fast, intermediate, or slow exchange range with respect to chemical shift can often be judged from the appearance of the spectrum. For fast exchange a single resonance line is observed, with a chemical shift that is a weighted average of the individual species:

$$\delta_{\text{obs}} = \alpha\delta_A + (1 - \alpha)\delta_B \quad (1.68)$$

where α is the fractional population of species A, for the equilibrium:



In the intermediate exchange region, either single or multiple resonances occur, with

Table 1.5 NMR methods for determining motional correlation times, τ_c

$1 \text{ s} < \tau_c$	Real-time monitoring after initial perturbation
$10 \text{ ms} < \tau_c < 10 \text{ s}$	Two- or three-dimensional exchange spectroscopy (EXSY)
$100 \text{ } \mu\text{s} < \tau_c < 1 \text{ s}$	Lineshape analysis, exchange broadening, and exchange narrowing
$1 \text{ } \mu\text{s} < \tau_c < 10 \text{ ms}$	Measurements of relaxation time $T_{1\rho}$ in the rotating frame
$30 \text{ ps} < \tau_c < 1 \text{ } \mu\text{s}$	Measurements of relaxation time T_1 in the laboratory frame
$\tau_c < 100 \text{ ps}$	Averaged order parameter values

Table 1.6

Timescale	Exchange rate		
	Slow	Intermediate	Fast
δ	$\tau \gg 1/ \delta_A - \delta_B $	$\tau \approx 1/ \delta_A - \delta_B $	$\tau \ll 1/ \delta_A - \delta_B $
J	$\tau \gg 1/ J_A - J_B $	$\tau \approx 1/ J_A - J_B $	$\tau \ll 1/ J_A - J_B $
$1/T_{(1 \text{ or } 2)}$	$\tau \gg 1/ 1/T_A - 1/T_B $ $\gg \left \frac{T_A T_B}{T_A - T_B} \right $	$\tau \approx 1/ 1/T_A - 1/T_B $ $\approx \left \frac{T_A T_B}{T_A - T_B} \right $	$\tau \ll 1/ 1/T_A - 1/T_B $ $\ll \left \frac{T_A T_B}{T_A - T_B} \right $

characteristic lineshapes. Typical spectra³¹ reflecting exchange at different rates relative to the chemical shift are shown in Fig. 1.50.

1.3.2 Slow and fast exchange

If a nucleus is changing between two or more environments, its resonance behaviour will be described by the Bloch equations only in the two extreme limits of slow and fast exchange. To take into account the intermediate region, in which exchange rates contribute to relaxation, the Bloch equations must be modified. For a simple two-site exchange, with $\delta_A \neq \delta_B$ but with no spin-spin coupling ($J_A = J_B = 0$), and with $T_{2A} = T_{2B} = T_2$, the modified Bloch equations, known as the McConnell equations, may be applied. Additional assumptions are that (i) the lifetime of the transition state is short, so that the exchange rate is determined by the lifetimes in either state, and that (ii) the rate of disappearance of nuclei from either environment follows first-order kinetics. The McConnell equations are:

$$\frac{d\mathbf{M}_{Ax}}{dt} = \gamma(\mathbf{M}_{Ax}\mathbf{B}_0 + \mathbf{M}_{Az}\mathbf{B}_1 \sin \omega t) - \frac{\mathbf{M}_{Ax}}{T_2} - \frac{\mathbf{M}_{Ax}}{\tau_A} + \frac{\mathbf{M}_{Bx}}{\tau_B} \quad (1.69)$$

$$\frac{d\mathbf{M}_{Ay}}{dt} = \gamma(\mathbf{M}_{Az}\mathbf{B}_1 \cos \omega t - \mathbf{M}_{Ax}\mathbf{B}_0) - \frac{\mathbf{M}_{Ay}}{T_2} - \frac{\mathbf{M}_{Ay}}{\tau_A} + \frac{\mathbf{M}_{By}}{\tau_B} \quad (1.70)$$

$$\frac{d\mathbf{M}_{Bx}}{dt} = \gamma(\mathbf{M}_{By}\mathbf{B}_0 + \mathbf{M}_{Bz}\mathbf{B}_1 \sin \omega t) - \frac{\mathbf{M}_{Bx}}{T_2} - \frac{\mathbf{M}_{Bx}}{\tau_B} + \frac{\mathbf{M}_{Ax}}{\tau_A} \quad (1.71)$$

$$\frac{d\mathbf{M}_{By}}{dt} = \gamma(\mathbf{M}_{Bz}\mathbf{B}_1 \cos \omega t - \mathbf{M}_{Bx}\mathbf{B}_1) - \frac{\mathbf{M}_{By}}{T_2} - \frac{\mathbf{M}_{By}}{\tau_B} + \frac{\mathbf{M}_{Ay}}{\tau_A} \quad (1.72)$$

where $\mathbf{M}_{A,B,x,y,z}$ is the expectation value for the bulk magnetization along a particular Cartesian axis in the rotating frame, \mathbf{B}_0 is the static magnetic field, \mathbf{B}_1 is the applied RF field, ω is the Larmor frequency, and τ_A and τ_B are the lifetimes of the nucleus in each site. Thus the total rate of change of the nuclear magnetization in state A will depend on the rate of change of the magnetization in state B. The general solution to the McConnell equations is rather complex:

$$f(\omega) = \frac{1}{2}\gamma\mathbf{M}_0 \frac{(1 + \tau/T_2) + QR}{P^2 + R^2} \quad (1.73)$$

where

$$\tau = \tau_A\tau_B/(\tau_A + \tau_B) \quad (1.74)$$

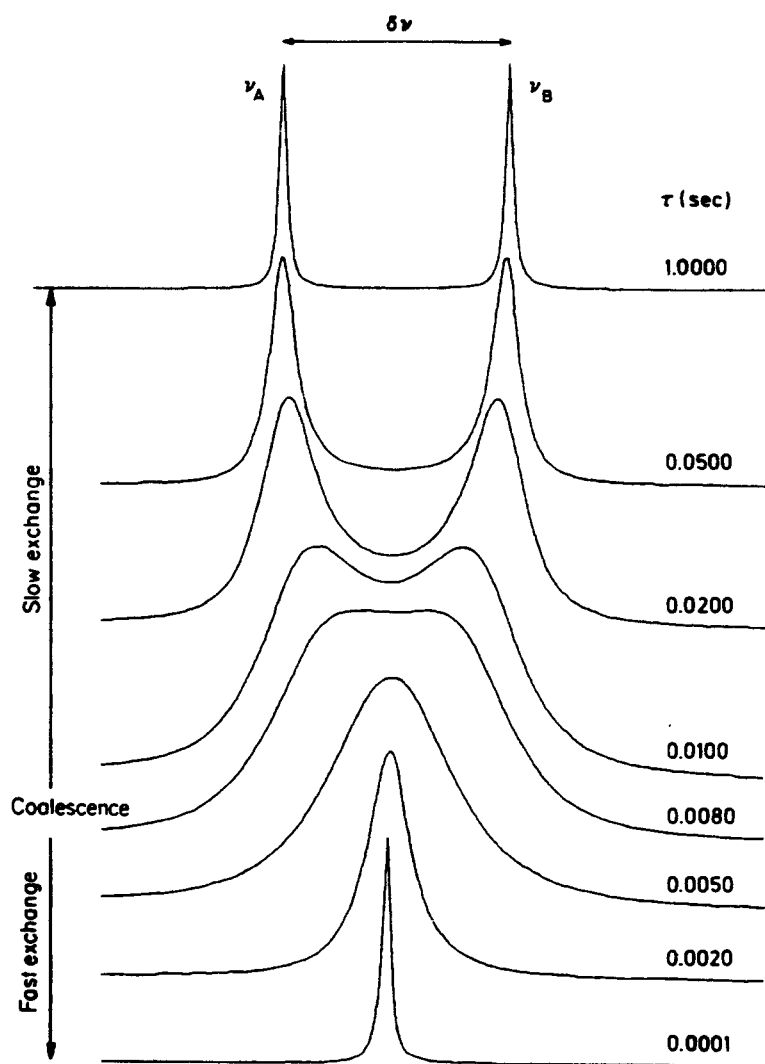


Fig. 1.50 Typical spectra reflecting exchange at different rates relative to the chemical shifts. (Reprinted from Ref. 31 with permission.)

is the mean lifetime, and

$$P = \tau(1/T_2)^2 - [\frac{1}{2}(\omega_A + \omega_B) - \omega]^2 + \frac{1}{4}(\omega_A - \omega_B)^2 + 1/T_2 \quad (1.75)$$

$$Q = \tau[\frac{1}{2}(\omega_A + \omega_B) - \omega - \frac{1}{2}(p_A - p_B)(\omega_A - \omega_B)] \quad (1.76)$$

$$R = [\frac{1}{2}(\omega_A + \omega_B) - \omega](1 + 2\tau/T_2) + \frac{1}{2}(p_A - p_B)(\omega_A - \omega_B) \quad (1.77)$$

where p_A and p_B are the fractional populations of nuclei A and B.

This rather complicated equation can be simplified considerably if we consider effective transverse relaxation rates of equally populated sites (which are related to linewidth) for slow exchange:

$$\frac{1}{T_{2\text{obs}}} = \frac{1}{T_{2A}} + k \quad (1.78)$$

and for fast exchange:

$$\frac{1}{T_{2\text{obs}}} = \frac{1}{T_2} + \frac{(\omega_A - \omega_B)^2}{8k_a} \quad (1.79)$$

If the sites are unequally populated, then for slow exchange (assuming $p_B \ll p_A \approx 1$):

$$\frac{1}{T_{2\text{obs}}} = \frac{1}{T_{2A}} + k_a p_B \quad (1.80)$$

and for fast exchange:

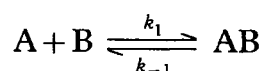
$$\frac{1}{T_{2\text{obs}}} = \frac{p_A}{T_{2A}} + \frac{p_B}{T_{2B}} + \frac{p_A p_B (\omega_A - \omega_B)^2}{k_a + k_b} \quad (1.81)$$

1.3.3 Intermediate and more complex exchange

In the case of intermediate exchange the general equations must be used for the calculations (Equation (1.73)). This is of course, more complicated and the reader is referred to a number of excellent texts on the detailed analysis of dynamic NMR spectra.³²⁻³⁴

1.3.4 Measuring rate constants

The value of measuring rate constants is that enzyme kinetics may be determined *in vitro* and also *in vivo*.³⁵ This may be achieved experimentally by determining either δ_A and δ_B , $1/T_{2A}$ and $1/T_{2B}$, or $1/T_{1A}$ and $1/T_{1B}$. For the latter two sets of parameters, the Carr–Purcell–Meiboom–Gill spin echo sequence, and the inversion–recovery sequence (and saturation transfer or NOESY) may be used respectively. Consider the example of ligand binding to a macromolecule:



Let the parameters being measured be P , so that

$$P_{\text{obs}} \approx P_A p_A + P_{\text{AB}} p_{\text{AB}} \quad (1.82)$$

where $p_A = [A]/A_{\text{total}}$, $p_{\text{AB}} = [AB]/A_{\text{total}}$, and $A_{\text{total}} = [A] + [AB]$ and $B_{\text{total}} = [B] + [AB]$. Let $\Delta_0 = P_{\text{AB}} - P_A$ and $\Delta = P_{\text{obs}} - P_A$. Since $p_A + p_{\text{AB}} = 1$,

$$\Delta = \Delta_0 p_{\text{AB}} \quad (1.83)$$

Also at equilibrium,

$$K_d = \frac{[A][B]}{[AB]} = \frac{k_{-1}}{k_1} \quad (1.84)$$

So we can write p_{AB} as:

$$\frac{[B]}{[B] + K_d} \quad \text{or} \quad \frac{[A]B_{\text{total}}}{A_{\text{total}}([A] + K_d)} \quad (1.85)$$

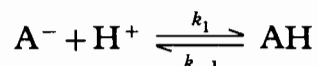
If the experiment is carried out at constant A_{total} , and B_{total} is varied, then

$$\Delta = \frac{\Delta_0[B]}{[B] + K_d} \quad (1.86)$$

which is of the same form as the Michaelis–Menten equation, so K_d can readily be determined. If A_{total} is varied, the equations are less simple, although if $[A] \gg [AB]$ then

$$\Delta = \frac{\Delta_0 B_{\text{total}}}{A_{\text{total}} + K_d} \quad (1.87)$$

Note that for the simple acid–base equilibrium:



the equation has the same form:

$$\Delta = \frac{\Delta_0[H^+]}{[H^+] + K_a} \quad (1.88)$$

so if Δ is plotted against pH, $pK_a = \text{pH}$ when $\Delta = \Delta_0/2$.

1.3.5 Saturation transfer

In the case of slow exchange, irradiation of resonance A will cause changes in intensity of the other resonances (B) because of *transfer of saturation* from one to the other as a result of exchange (provided that the exchange rate is comparable to the longitudinal relaxation rate $1/T_1$). This is exactly analogous to the NOE, and a one-dimensional saturation transfer experiment is analogous to the one-dimensional NOE difference experiment. The fractional change in intensity of the B resonance is given by the equation:

$$\frac{I_{\text{B}'}}{I_{\text{B}}} = \frac{1/T_{1\text{B}}}{1/T_{1\text{B}} + k_b} \quad (1.89)$$

where I_B and $I_{B'}$ are the intensities of the B resonance before and after irradiation of the A resonance respectively. Note that

$$\frac{1}{T_{\text{obs}}} = \frac{1}{T_{1A}} + \frac{p_B k_b}{T_{1B}} \quad (1.90)$$

An example is shown in Fig. 1.51.

1.3.6 Two-dimensional exchange spectroscopy

The two-dimensional NOESY pulse sequence may be used to measure cross-relaxation due to chemical exchange as well as due to dipolar coupling. The pulse sequence is essentially identical to the NOESY although the name EXSY (for EXchange Spectroscopy) has been argued to be more appropriate for this usage³⁶. An example is shown in Fig. 1.52. The cross-peak intensities may be used to calculate site-to-site rate constants, although the intensities need to be evaluated as a function of τ_m (mixing time):

$$I_{ij}(\tau_m) = [\delta_{ij} - \tau_m R_{ij} + \frac{1}{2} \tau_m^2 \sum_k R_{ik} R_{kj} - \dots] M_j^0 \quad (1.91)$$

where M_j^0 refers to the initial magnetization of j , $R_{ij} = -k_{ji}$, and are off-diagonal elements of the exchange matrix (\mathbf{R}), whose diagonal elements are $R_{ii} = T_{1,i}^{-1} + \sum_j k_{ij}$. This matrix contains all the site-to-site rate constants. Furthermore $I_{ij} = I_{ji}$ even if $R_{ij} \neq R_{ji}$, which implies that the two-dimensional EXSY spectrum must be symmetric about the diagonal, and that unequal populations do *not* lead to asymmetry. At short mixing times, Equation (1.91) simplifies to:

$$I_{ij}(\tau_m) \approx -\tau_m R_{ij} M_j^0 = k_{ji} \tau_m M_j^0 \quad (1.92)$$

for $i \neq j$. Now the two-dimensional spectrum becomes a graphic display directly

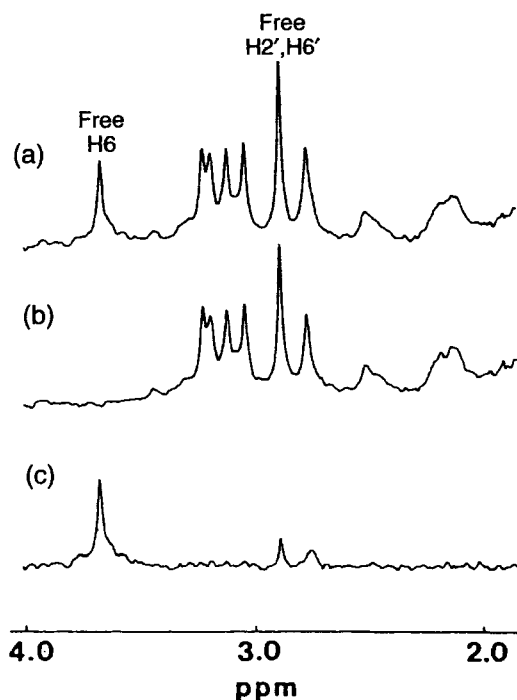


Fig. 1.51 One-dimensional saturation transfer ^1H NMR spectra of dihydrofolate reductase (a) without irradiation; (b) with irradiation at the resonance frequency of the 6-proton in the enzyme-free ligand trimethoprim; and (c) the difference spectrum (showing resonances due to the 6-proton of the enzyme-bound ligand trimethoprim, which is relatively broad, and within the free ligand). (Reprinted from Cayley *et al.*, *Biochemistry*, **18**, 3886 (1979) with permission.)

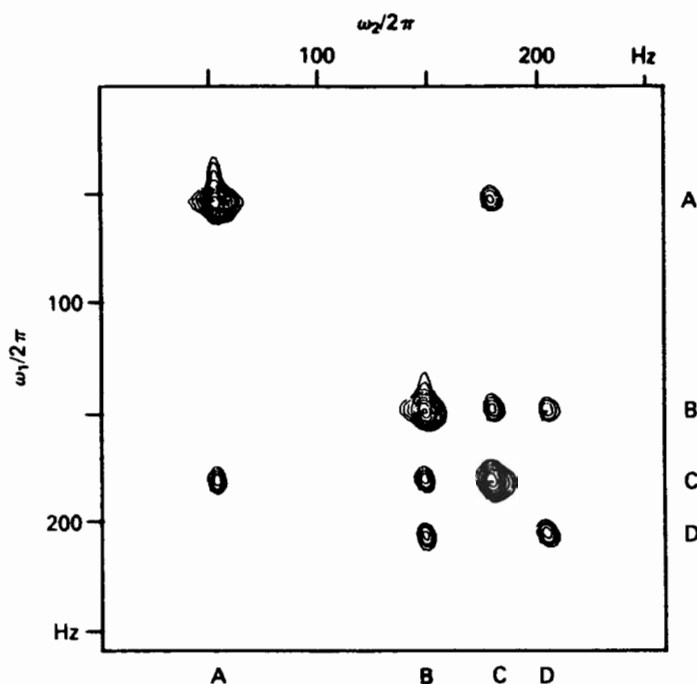


Fig. 1.52 Two-dimensional exchange spectrum of the protons in heptamethyl benzenonium ion in 9.4 M H_2SO_4 . (Reprinted from Ref. 4 with permission.)

proportional to the exchange matrix \mathbf{R} . The complexity of the exact equation (1.91) arises because cross-peaks between i and j can arise indirectly, by exchange from i to k and from k to j before the mixing period has expired. However, at very short τ_m these indirect cross-peaks vanish, so that the equations simplify. Equation (1.92) therefore permits solving for the rate constants, but it is inherently inaccurate, since at short values of τ_m the cross-peak intensities are small and therefore difficult to measure. Furthermore, at τ_m values that are practical, there is a risk of indirect cross-peaks which could be mistaken for evidence for a direct exchange process. A solution to this is to use several short τ_m values and determine k_{ij} as the slope of a plot of $I_{ij}(\tau_m)$ versus $M_j^0 \tau_m$. This distinguishes direct cross-peaks, which have a non-zero slope, from the indirect ones, which show zero slope. However multiple τ_m experiments can consume large amounts of instrument time and using the general solution to Equation (1.91) is preferable. For simple two-site exchange between two uncoupled systems of spins A and B, assuming equal populations and $T_{1,A} = T_{1,B} = T_1$, and exchange rate constant, $k = k_{AB} + k_{BA}$, the intensities of the diagonal peaks and cross-peaks reduce to:

$$k = \frac{1}{\tau_m} \ln \frac{r+1}{r-1} \quad (1.93)$$

where $r = (I_{AA} + I_{BB}) / (I_{AB} + I_{BA})$, or with unequal populations $r = 4p_A p_B (I_{AA} + I_{BB}) / (I_{AB} + I_{BA}) - (p_A - p_B)^2$. By simply knowing the cross-peak intensity ratio, the rate constant for chemical exchange can be calculated. Of course, the great value of the two-dimensional experiment is its ability to measure multisite exchange rate constants, for which the two-site approximation is of no help, and the more complex matrix analysis is required (see Section 3.8).

An alternative approach to the EXSY experiment, which is effectively a three-dimensional NMR experiment (the three time variables being t_1 , t_2 , and τ_m), is the

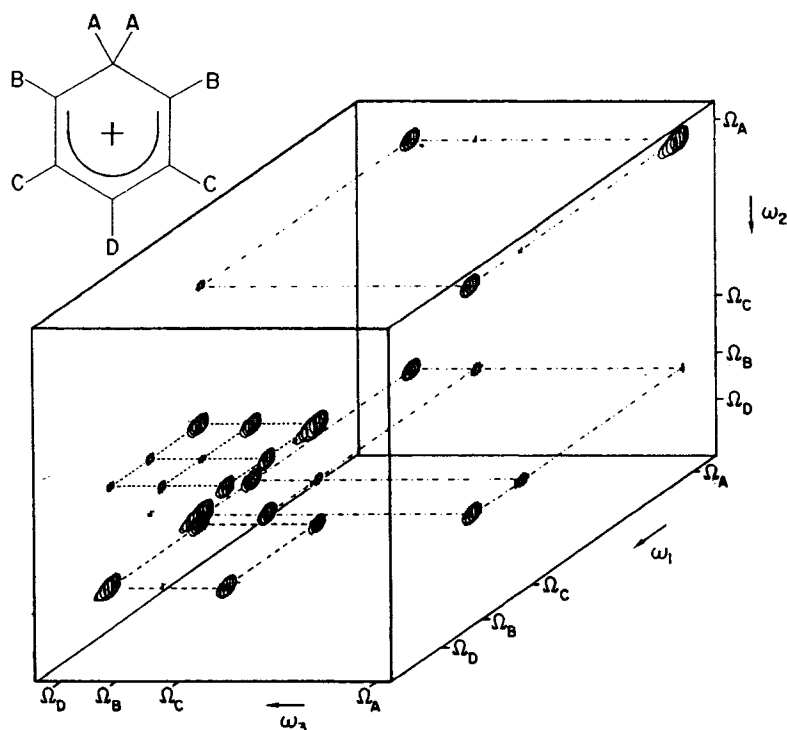


Fig. 1.53 Three-dimensional EXSY-EXSY of heptamethylbenzenonium ion in sulphuric acid. Peaks that lie on identical planes (ω_1, ω_3) are connected by lines. (Reprinted from Ref. 38 with permission.)

so-called 'ACCORDION' experiment, in which t_1 and τ_m are varied together, thus reducing the experiment to a two-dimensional experiment.³⁷ The full three-dimensional EXSY-EXSY experiment can also be used as illustrated in Fig. 1.53 for heptamethylbenzenonium sulphate in sulphuric acid. The possible exchange processes are due to the 1,2 methyl group shifts: $A \rightleftharpoons B$, $B \rightleftharpoons C$, and $C \rightleftharpoons D$.³⁸

1.4 MOLECULAR MOTION

1.4.1 Temperature dependence of chemical shifts

Note that *prima facie* it is not easy to tell if a particular line is affected by chemical exchange or not, particularly when approaching fast exchange. Thus it will not necessarily be obvious from examination of the resonances in a ^1H NMR spectrum of a protein whether a particular line is exchange broadened or shifted. Such exchange might be due to exchange with solvent, exchange from ionization, exchange from ligand binding, or exchange from conformational equilibria. Examination of the temperature dependence of the spectrum can help to reveal exchange, and furthermore may be used to examine molecular dynamics, for example the flipping of an aromatic ring (see Fig. 1.54).

1.4.2 Use of relaxation rates and NOEs

T_1 s, T_2 s, and NOEs may be used for measuring molecular motion in the form of local librational motion. For example, when ^{13}C T_1 measurements were made on sonicated dipalmitoyl lecithin suspensions, the results shown in Fig. 1.55 were obtained. The relaxation is dominated by the dipolar interaction from the hydrogens on the same bond. Apart from the carboxyls, which have no attached hydrogens, there is an increase in T_1 , both towards the CH_3 group and towards the $(\text{CH}_3)_3\text{N}^+$ group. This means that there is increased mobility towards the ends of these chains.

where the denominator is a normalizing factor and $\langle \omega \rangle$ is the mean angular frequency of the line:

$$\langle \omega \rangle = \frac{\int_{-\infty}^{\infty} \omega f(\omega) d\omega}{\int_{-\infty}^{\infty} f(\omega) d\omega} \quad (1.95)$$

If $f(\omega)$ is an even function of ω , $M_j = 0$ for all odd j , as is the case for dipolar interactions in high magnetic fields. Usually only the second moment, M_2 is used. Thus the moment of a curve is its mean squared width.

The importance of the second moment lies in the fact that it may be calculated theoretically if the lattice positions of the nuclei are known. The pairwise interactions summed over the lattice for a single crystal are described by M_2 , which for a dipolar interaction is given by:

$$M_2(\text{heteronuclear}) = [\frac{1}{2}(2\pi D)(1 - 3 \cos^2 \theta)]^2 \quad (1.96)$$

$$M_2(\text{homonuclear}) = [\frac{3}{4}(2\pi D)(1 - 3 \cos^2 \theta)]^2 \quad (1.97)$$

where D is the dipolar coupling constant, or, more generally:

$$M_2(\text{heteronuclear}) = \left(\frac{1}{2} \gamma_A \gamma_B \hbar \frac{\mu_0}{4\pi} \right)^2 \sum_k \left[(1 - 3 \cos^2 \theta_{jk})^2 / r_{jk}^6 \right] \quad (1.98)$$

$$M^2(\text{homonuclear}) = \left(\frac{3}{4} \gamma^2 \hbar \frac{\mu_0}{4\pi} \right)^2 \sum_k \left[(1 - 3 \cos^2 \theta_{jk})^2 / r_{jk}^6 \right] \quad (1.99)$$

where the sum runs over all relevant nuclei, k , in relation to the considered nucleus j . As we have discussed before, any rapid molecular motions will tend to partially average the dipolar interactions, so the second moment will appear to be decreased below its rigid

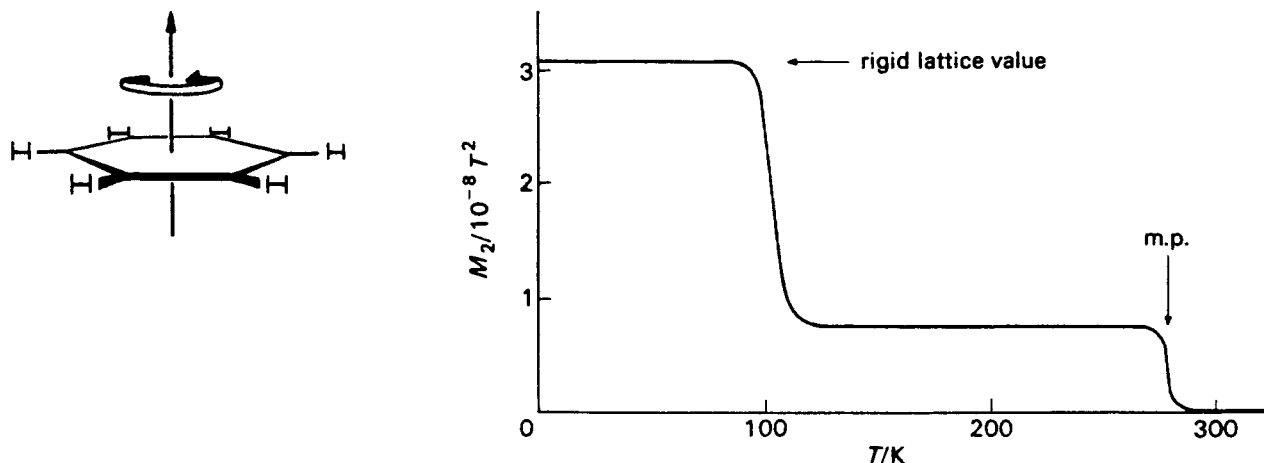


Fig. 1.56 Variation of the intramolecular homonuclear contribution to the second moment of the proton resonance of benzene as a function of temperature. (Reprinted from Ref. 39 with permission.)

lattice value. Consider a simple molecular motion such as rotation about an axis fixed in the molecule, for example the proton spectrum of solid benzene rotating about the plane of the ring is shown in Fig. 1.56.

The variation of M_2 with temperature is also shown in Fig. 1.56.³⁹ Some molecular motion at ≈ 100 K causes a reduction in the second moment (by a factor of 4). Incidentally, a moment analysis can be used to obtain the chemical-shift anisotropy parameters $\delta(=(\sigma_{33}-\sigma_1))$ and $\eta(=(\sigma_{11}-\sigma_{22})/(\sigma_{33}-\sigma_1))$:

$$M_2 = (\delta^2/15)(3 + \eta^2) \quad (1.100)$$

and the third moment,

$$M_3 = (2\delta^3/35)(1 - \eta^2) \quad (1.101)$$

1.4.4 Quadrupolar nuclei

One of the problems of solid-state ^2H NMR is the high RF powers that are involved, and the possibility of distortion to the spectra as a result of what is known as 'breakthrough' (which is the receiver detecting the end of the transmitter pulse, since at high power levels it takes some time for the RF coil to dissipate the power). One pulse sequence which helps in this area is related to the Hahn spin echo sequence, and is called the quadrupolar echo sequence:

$$(\pi/2)_x - \tau - (\pi/2)_y - 2\tau - t_2 \text{---(acquisition)}$$

Unfortunately, because spin-1 nuclei have three available spin states, it is not possible to represent the behaviour of the spins in terms of simple magnetization vectors as is possible for spin- $\frac{1}{2}$ nuclei. However, the effect of the sequence is highly analogous to the Hahn spin echo sequence for spin- $\frac{1}{2}$ nuclei. The time-dependent behaviour of the spins is reversed and the spins are refocused to give an echo. The important feature of this application of echo formation is that the loss of critical data points from the beginning of the FID (caused by the receiver dead-time and pulse breakthrough) is avoided in the echo, which is well removed in time from the RF pulse. Since these initial data points are crucial in defining the outer limits of the spectrum, a dramatic improvement in spectral lineshape is observed (see Fig. 1.57).

When molecular motion is present, the situation can become more complex, and the detailed spectral shape may be dependent on the pulse interval used to produce the echo (2τ), and may be used to ascribe a mechanism to the motion.



Fig. 1.57 Spectra of perdeuterated Perspex (plexiglass) illustrating the effect of the quadrupolar echo sequence. (a) Spectrum obtained using $\pi/2$ pulses. (b) Spectrum obtained with quadrupolar echo sequence. (Reprinted from Ref. 28 with permission.)

REFERENCES

1. B. Jacobson, W. A. Anderson, and J. T. Arnold, *Nature*, **17**, 772–3 (1954).
2. M. Saunders, A. Wishnia, and J. G. Kirkwood, *J. Am. Chem. Soc.*, **79**, 3289 (1957).
3. A. Abragam, *Principles of Nuclear Magnetism*, Oxford University Press (1961).
4. R. R. Ernst, G. Bodenhausen, and A. Wokaun, *Principles of Nuclear Magnetic Resonance in One and Two Dimensions*, Oxford University Press (1987).
5. D. M. S. Bagguley (ed.), *Pulsed Magnetic Resonance: NMR, ESR, and Optics (A Recognition of E. L. Hahn)* Oxford University Press (1992).
6. C. P. Slichter, *Principles of Magnetic Resonance*, 2nd edn, Springer-Verlag, Berlin (1978).
7. A. E. Derome, *Modern NMR Techniques for Chemistry Research*, Pergamon, Oxford (1987).
8. J. K. M. Sanders and B. K. Hunter, *Modern NMR Spectroscopy, A Guide for Chemists*, 2nd edn, Oxford University Press (1993).
9. R. A. Dwek, *NMR in Biochemistry*, Clarendon Press, Oxford (1973).
10. T. L. James, *Nuclear Magnetic Resonance in Biochemistry*, Academic Press, New York (1975).
11. K. Wüthrich, *NMR in Biological Research: Peptides and Proteins* American Elsevier, New York (1976).
12. O. Jardetsky and G. C. K. Roberts, *NMR in Molecular Biology*, Academic Press, New York (1981).
13. K. Wüthrich, *NMR of Proteins and Nucleic Acids* John Wiley and Sons, New York (1986).
14. P. G. Morris, *NMR Imaging in Medicine and Biology*, Oxford University Press (1986).
15. L. Kaufman, L. E. Crooks, and A. R. Margulis, *NMR Imaging in Medicine*, Igakun-shoin, Tokyo (1981).
16. J. W. Shriver, *J. Magn. Reson.*, **94**, 612 (1991).
17. P. Güntert, N. Schaefer, G. Otting, and K. Wüthrich, *J. Magn. Reson. Series A*, **101**, 103–5 (1993).
18. See, for example: G. W. Vuister, R. Boelens, R. Kaptein, R. E. Hurd, B. John, and P. C. M. Van Zijl, *J. Am. Chem. Soc.*, **113**, 9688–90 (1991) and references cited therein.
19. O. W. Sørensen, G. W. Eich, M. H. Levitt, G. Bodenhausen, and R. R. Ernst, *Prog. in NMR Spectros.*, **16**, 163–92 (1983).
20. R. G. Brewer and E. L. Hahn, *Sci Am.*, **251**, 50–7 (1984).
21. I. Solomon, *Phys. Rev.*, **99**, 559 (1955).
22. D. Neuhaus and M. Williamson, *The Nuclear Overhauser Effect in Structural and Conformational Analysis*, VCH Publishers, New York (1989).
23. M. Karplus, *J. Chem. Phys.*, **30**, 11 (1959).
24. M. Karplus, *J. Am. Chem. Soc.*, **85**, 2870 (1963).
25. M. Mehring, *High Resolution NMR in Solids*, 2nd edn, Springer-Verlag, New York (1983).
26. U. Haeberlin, *High Resolution NMR in Solids: Selective Averaging*, Academic Press, New York (1976).
27. B. C. Gerstein and C. R. Dybrowski, *Transient Techniques in NMR of Solids*, Academic Press, Orlando FL (1985).
28. C. A. Fyfe, *Solid State NMR for Chemists*, CFC Press, Guelph (1983).
29. W. T. Dixon, *J. Magn. Reson.*, **44**, 220 (1981).
30. J. Herzfeld and A. E. Berger, *J. Chem. Phys.*, **73**, 6021–30 (1980).
31. H. Günther, *NMR Spectroscopy*, John Wiley and Sons, New York (1980).
32. L. M. Jackman and F. A. Cotton (eds.) *Dynamic NMR Spectroscopy*, Academic Press, New York (1975).
33. J. L. Kaplan and G. Fraenkel, *NMR of Chemically Exchanging Systems*, Academic Press, New York (1980).
34. J. Sandström, *Dynamic NMR Spectroscopy*, Academic Press, New York (1982).
35. K. M. Brindle, *Prog. in NMR Spectroscopy*, **20**, 257–93 (1988).
36. C. L. Perrin and T. J. Dwyer, *Chem. Rev.*, **90**, 935–67 (1990).
37. G. Bodenhausen and R. R. Ernst, *J. Am. Chem. Soc.*, **104**, 1304 (1982).
38. C. Griesinger, O. W. Sørensen, and R. R. Ernst, *J. Magn. Reson.*, **84**, 14–63 (1989).
39. E. R. Andrew and R. G. Eades, *Proc. Roy. Soc. A.*, **218**, 537 (1953).